

## Iron overload causes endolysosomal deficits modulated by NAADP-regulated 2-pore channels and RAB7A

Belén Fernández<sup>a</sup>, Elena Fdez<sup>a</sup>, Patricia Gómez-Suaga<sup>a</sup>, Fernando Gil<sup>b</sup>, Isabel Molina-Villalba<sup>b</sup>, Isidro Ferrer<sup>c</sup>, Sandip Patel<sup>d</sup>, Grant C. Churchill<sup>e</sup>, and Sabine Hilfiker<sup>a</sup>

<sup>a</sup>Institute of Parasitology and Biomedicine “López-Neyra,” Consejo Superior de Investigaciones Científicas (CSIC), Granada, Spain; <sup>b</sup>Department of Legal Medicine and Toxicology, School of Medicine, University of Granada, Granada, Spain; <sup>c</sup>Institute of Neuropathology, IDIBELL-University Hospital Bellvitge, University of Barcelona, Llobregat, Spain; <sup>d</sup>Department of Cell and Developmental Biology, University College London, London, UK; <sup>e</sup>Department of Pharmacology, University of Oxford, Oxford, UK

### ABSTRACT

Various neurodegenerative disorders are associated with increased brain iron content. Iron is known to cause oxidative stress, which concomitantly promotes cell death. Whereas endolysosomes are known to serve as intracellular iron storage organelles, the consequences of increased iron on endolysosomal functioning, and effects on cell viability upon modulation of endolysosomal iron release remain largely unknown. Here, we show that increasing intracellular iron causes endolysosomal alterations associated with impaired autophagic clearance of intracellular protein aggregates, increased cytosolic oxidative stress and increased cell death. These effects are subject to regulation by NAADP, a potent second messenger reported to target endolysosomal TPCNs (2-pore channels). Consistent with endolysosomal iron storage, cytosolic iron levels are modulated by NAADP, and increased cytosolic iron is detected when overexpressing active, but not inactive TPCNs, indicating that these channels can modulate endolysosomal iron release. Cell death triggered by altered intralysosomal iron handling is abrogated in the presence of an NAADP antagonist or when inhibiting RAB7A activity. Taken together, our results suggest that increased endolysosomal iron causes cell death associated with increased cytosolic oxidative stress as well as autophagic impairments, and these effects are subject to modulation by endolysosomal ion channel activity in a RAB7A-dependent manner. These data highlight alternative therapeutic strategies for neurodegenerative disorders associated with increased intracellular iron load.

### ARTICLE HISTORY

Received 26 June 2015  
Revised 5 May 2016  
Accepted 11 May 2016

### KEYWORDS

iron; lysosome; NAADP; neurodegeneration; RAB7A; TPCN1; TPCN2

### Introduction

Whereas iron is an essential element for many biological processes, increases in intracellular iron cause cellular damage through hydroxyl radical production. Accumulation of iron occurs in many neurodegenerative diseases, and is especially pronounced in the basal ganglia, which may explain the association of increased iron with a variety of movement disorders including Parkinson disease.<sup>1,2</sup> It remains unclear whether iron accumulation is a primary event, or secondary to the neurodegenerative process. However, as iron accumulation also occurs during healthy aging, and as aging is a major risk factor for neurodegeneration, iron dyshomeostasis likely plays an important role in the mechanisms underlying cellular demise.

Within cells, iron can be incorporated into the intracellular labile iron pool and iron-containing proteins, stored in ferritin as a soluble, nontoxic form, or stored in endolysosomes.<sup>1,3,4</sup> Interestingly, numerous neurodegenerative diseases including Parkinson disease are associated with lysosomal dysfunction,<sup>5</sup> suggesting the possibility that iron overload may be a contributing factor. However, the precise cellular events triggered by endolysosomal iron

dyshomeostasis, and the iron release channels responsible for modulating metal homeostasis remain unclear.

Endolysosomes contain a variety of cation channels including TPCN1 (2-pore channel 1) and TPCN2, and MCOLN1 (mucolipin 1)/TRPML1, MCOLN2/TRPML2 and MCOLN3/TRPML3, respectively. Both TPCN and MCOLN channels are known to function as calcium release channels with roles in endolysosomal transport and fusion processes.<sup>6–8</sup> However, they can also conduct ions other than calcium, with TPCN1 and TPCN2 also reported to be permeable to sodium,<sup>9,10</sup> and MCOLN1 and MCOLN2 permeable to iron and zinc,<sup>11,12</sup> indicating that these channels may play a more general role in controlling cation and heavy metal homeostasis in endolysosomal organelles.<sup>13</sup>

In this study we show that cellular iron overload is associated with endolysosomal deficits, autophagic impairments, enhanced cytosolic oxidative stress and cell death. These effects are regulated by TPCN channels in a manner sensitive to NAADP and a highly selective NAADP antagonist,<sup>28</sup> as well as to RAB7A activity. These findings have broad implications for our understanding of

**CONTACT** Sabine Hilfiker  [sabine.hilfiker@ipb.csic.es](mailto:sabine.hilfiker@ipb.csic.es)

Color versions of one or more of the figures in the article can be found online at [www.tandfonline.com/kaup](http://www.tandfonline.com/kaup).

 Supplemental data for this article can be accessed on the [publisher's website](http://www.tandfonline.com/kaup).

© 2016 Belén Fernández, Elena Fdez, Patricia Gómez-Suaga, Fernando Gil, Isabel Molina-Villalba, Isidro Ferrer, Sandip Patel, Grant C. Churchill, and Sabine Hilfiker. Published with license by Taylor & Francis.

This is an Open Access article distributed under the terms of the Creative Commons Attribution-Non-Commercial License (<http://creativecommons.org/licenses/by-nc/3.0/>), which permits unrestricted non-commercial use, distribution, and reproduction in any medium, provided the original work is properly cited. The moral rights of the named author(s) have been asserted.

intracellular iron handling and provide novel insights into possible innovative modifying therapies for common neurodegenerative diseases involving iron dyshomeostasis.

## Results

### *Increased intracellular iron mediates cytotoxicity and oxidative stress*

We analyzed iron levels in postmortem samples from control and Lewy body disease patients. A significant increase in total iron content was observed in substantia nigra samples from patients with disease as compared to age-matched controls, consistent with previous studies reporting increased iron load in distinct neurodegenerative diseases (Fig. 1A).<sup>29-31</sup>

In serum, iron is found in highly soluble form, and bound to the iron transport protein transferrin (Tf). Tf binds  $\text{Fe}^{3+}$ , which allows it to bind to TFRC (transferrin receptor), followed by receptor-mediated endocytosis,<sup>32</sup> and such Tf-mediated  $\text{Fe}^{3+}$  uptake also seems to play a crucial role for neuronal iron acquisition.<sup>33</sup> Once in the acidic lumen of endolysosomes, iron is subsequently released from Tf as  $\text{Fe}^{2+}$ , and reduced iron transported across the endolysosomal membrane into the cytosol.<sup>34</sup> To model alterations in iron homeostasis in vitro, we employed ferric ammonium citrate (FAC) which has been reported to increase intracellular iron levels both in vitro and in vivo, concomitant with increased cell death.<sup>35,36</sup> Indeed, treatment of HEK293T cells with FAC caused a dose-dependent increase in total cellular iron content (Fig. 1B), and treatment of a variety of distinct cell types caused a dose- and time-dependent increase in apoptosis (Fig. 1C to F). The extent of cell death induced by increased intracellular iron load was similar among distinct cell lines, but more pronounced in cells with dopaminergic features such as PC12 or SH-SY5Y cells (Fig. S1). A dose- and time-dependent increase in apoptosis was also observed when increasing intracellular iron by application of  $\text{FeCl}_2$ , which becomes rapidly oxidized ( $\text{Fe}^{3+}$ ) (Fig. 1G). Moreover, the FAC-mediated increase in cell death was abolished when treating cells with dynasore (a cell-permeable dynamin inhibitor),<sup>37</sup> confirming that receptor-mediated endocytosis is largely responsible for iron uptake in our cultured cell systems (Fig. S2).

Chelatable iron can potentially induce oxidative stress, as it converts hydrogen peroxide to highly reactive hydroxyl radicals via the Fenton reaction. Indeed, FAC treatment caused a dose-dependent increase in the level of oxidized proteins (protein carbonyls) as analyzed by the oxyblot assay (Fig. 2A, B). In addition, transfection of cells with a reduction-oxidation-sensitive green fluorescent protein (ro-GFP) to allow for real time visualization of the oxidation state of the indicator<sup>38</sup> showed that FAC treatment caused a dose-dependent increase in the cytosolic oxidation state in living cells, similar to treatment with hydrogen peroxide (Fig. 2C, D).

### *Iron-mediated stress impairs autophagic clearance and causes endolysosomal alterations*

As oxidative stress induces autophagy,<sup>39</sup> we analyzed FAC-mediated autophagy induction in MAP1LC3B/GFP-LC3B-transfected cells (Fig. 3A). Increasing intracellular iron by either FAC or  $\text{FeCl}_2$  caused a significant, dose- and time-dependent accumulation of autophagosomes (Fig. 3B, C), and

western blotting for endogenous proteins from FAC or  $\text{FeCl}_2$ -treated cells indicated an increase in the levels of LC3B-II as well as SQSTM1/p62, a classical macroautophagy substrate (Fig. 3D, E).<sup>40</sup>

To more precisely determine how iron overload may affect autophagic flux, we employed a pH-sensitive tagged LC3B construct consisting of a tandem fusion of the red, acid-insensitive mCherry and the acid-sensitive GFP (td-tag-LC3B).<sup>41</sup> Td-tag-LC3B emits yellow (green merged with red) fluorescence in nonacidic structures (autophagosomes), but will appear as red only in autolysosomes due to the quenching of GFP in the acidic environment (Fig. 3F, G). Inducing autophagic flux by application of torin 1<sup>42</sup> caused a pronounced increase in both early and late autophagic structures (Fig. 3G). In contrast, treatment of cells with either FAC or  $\text{FeCl}_2$  significantly increased the percentage of yellow puncta, indicating an impairment in autophagic maturation (Fig. 3G).

To obtain further evidence for a FAC-mediated deficit in productive autophagy, cells were transfected with mutant polyglutamine-expanded HTT (huntingtin) fragment ( $\text{HTT}^{\text{Q74}}$ ), an aggregate-prone protein that can be employed as an exogenous reporter for protein homeostasis.<sup>43</sup> Simultaneous FAC treatment was found to cause an increase in the percentage of transfected cells with  $\text{HTT}^{\text{Q74}}$  aggregates (Fig. 4A, B). Whereas the presence of  $\text{HTT}^{\text{Q74}}$  on its own was not detrimental to cell survival, it aggravated cell death in the presence of iron overload (Fig. 4C). Thus, increasing intracellular iron content seems to be associated with a deficit in the autophagic clearance of aggregate-prone proteins and increased cell death, mechanistically mimicking events associated with various neurodegenerative disorders.<sup>44-49</sup>

To determine how iron overload and protein aggregation may mutually affect each other, we preincubated cells either in the absence or presence of FAC for 24 h, followed by  $\text{HTT}^{\text{Q74}}$  expression in the absence of FAC. Cells pretreated with FAC displayed an increase in protein aggregation as compared to untreated cells, which was paralleled by an increase in cell death (Fig. 4D). Conversely, we transfected cells with  $\text{HTT}^{\text{Q74}}$  and challenged them with or without FAC for the last 24 h of expression. Under these conditions, cells challenged with FAC also displayed increased protein aggregation associated with increased cell death (Fig. 4E). Thus, iron overload is able to sensitize cells for subsequent protein aggregation, while also able to enhance existing protein aggregation.

Lysosomes play critical roles in cellular homeostasis, and numerous neurodegenerative diseases are associated with a dysfunction of these organelles, often associated with compensatory lysosome proliferation.<sup>5</sup> Indeed, augmenting intracellular iron load was found to increase both the number and size of lysosomes as indicated by staining against LAMP2 (Fig. 5A to C), or by determining total LAMP2 content by western blotting (Fig. 5D). Similar results were observed in cells transfected with LAMP1-GFP, a late endosomal/endolysosomal marker (Fig. 5E to I).<sup>50</sup> Interestingly, FAC treatment not only increased the number and size of endolysosomes and total LAMP1 content as determined by western blotting (Fig. 5D), but also caused the appearance of very large endolysosomal structures (Fig. 5H, I).

Apart from the observed impairment in autophagic flux associated with a decrease in the clearance of protein

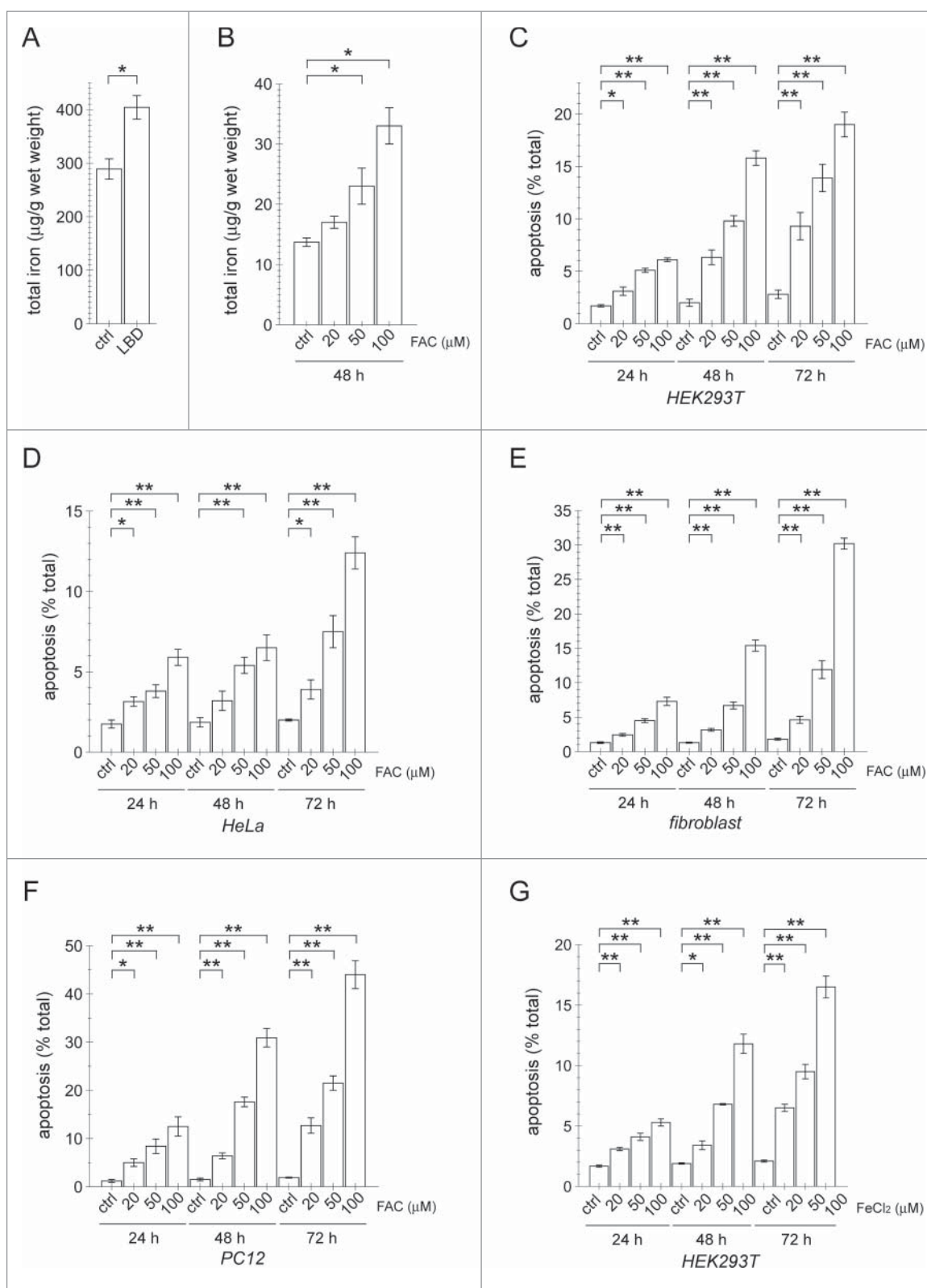


**Figure 1.** Increased iron is associated with neurodegeneration in vivo and mediates cytotoxicity in vitro. (A) Total iron levels (normalized to tissue wet weight) of substantia nigra samples from age-matched control and Lewy-body disease patients (LBD) as analyzed by atomic absorption spectroscopy. Graph represents mean  $\pm$  SEM ( $n = 5$ ; \*,  $P < 0.05$ ). (B) Total iron levels as analyzed by atomic absorption spectroscopy from HEK293T cells left either untreated (ctrl), or treated with the indicated concentrations of FAC for 48 h. Graph represents mean  $\pm$  SEM ( $n = 3$ ; \*,  $P < 0.05$ ). FAC treatment causes a time- and dose-dependent increase in apoptosis in HEK293T cells (C), HeLa cells (D), primary dermal fibroblasts (E) or dopaminergic PC12 cells (F). (G) FeCl<sub>2</sub> treatment causes a time- and dose-dependent increase in apoptosis in HEK293T cells. Graphs represent mean  $\pm$  SEM ( $n = 3$ ; \*,  $P < 0.05$ , \*\*,  $P < 0.005$ ).

aggregates, additional evidence for endolysosomal dysfunction was obtained by measuring endolysosomal pH by acridine orange (AO), a lysosomotropic metachromatic fluorochrome

which accumulates in acidic organelles, shifting its emission to longer wavelengths.<sup>51,52</sup> When excited with blue light, AO emits red fluorescence at high concentrations (in acidic

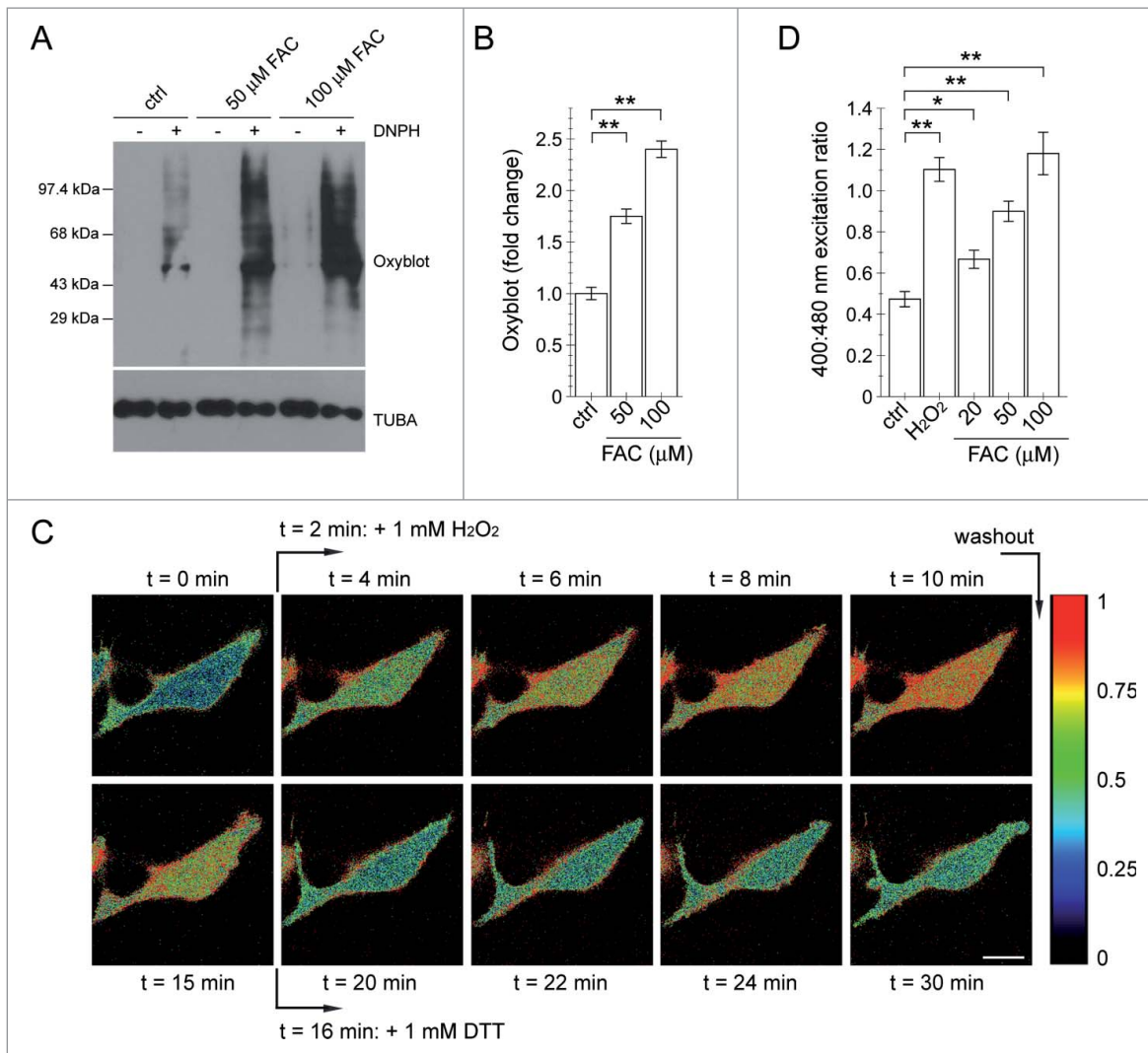


**Figure 2.** Increased iron load causes oxidative damage. (A) Oxyblot assay performed on HEK293T cells in the absence (ctrl) or presence of FAC treatment as indicated. DNP, 2,4-dinitrophenylhydrazine. (B) Oxyblot levels were quantified (fold change as compared to control), and bars represent mean  $\pm$  SEM ( $n = 3$ ; \*\*,  $P < 0.005$ ). (C) Representative experiment detecting oxidation in HEK293T cells upon addition of hydrogen peroxide, and reversal by DTT. Images were taken using an emission wavelength of 535 nm and 400 nm and 480 nm excitation wavelengths. Images were taken at 1 min intervals, and ratiometric values are depicted in pseudocolor calibrated using the color scale on the right. Concentration of chemicals and times of addition are indicated by arrows. Scale bar: 10  $\mu\text{m}$ . (D) Quantification of oxidation induced by either hydrogen peroxide or increasing concentrations of FAC applied during 48 h, respectively. Bars represent mean  $\pm$  SEM ( $n = 3$ ; \*,  $P < 0.05$ , \*\*,  $P < 0.005$ ).

organelles), and green fluorescence at low concentrations (in cytosol and nucleus). The number of AO-loaded acidic organelles per cell was almost entirely abolished when dissipating endolysosomal pH by either bafilomycin A<sub>1</sub> (BAF) or nigericin, and was significantly reduced upon treatment of cells with either FAC or FeCl<sub>2</sub> (Fig. 6A,B). Together, these data indicate that cellular iron overload causes both structural and functional changes in endolysosomal organelles.

#### Iron-mediated alterations are regulated by NAADP and TPCN channels

We next aimed to determine whether there is a possible link between increased intracellular iron, endolysosomal deficits and TPCN channels, known to be sensitive to a cell-permeant version of NAADP (NAADP-AM) and the NAADP antagonist Ned-19.<sup>20,28</sup> Whereas NAADP-AM or Ned-19 were without effect in the absence of increasing intracellular iron load,

NAADP-AM potentiated the effects of FAC or FeCl<sub>2</sub> on apoptotic cell death (Fig. 7A, B), cytosolic oxidation state (Fig. 7C) and autophagosome accumulation (Fig. 7D, E). The percentage of cells with HTT<sup>Q74</sup> aggregates and concomitant enhanced cell death was similarly potentiated (Fig. 7F), as was the number and size of endolysosomal structures induced upon FAC treatment (Fig. S3). Conversely, Ned-19 abolished all the iron overload-mediated effects (Fig. 7A to G, Fig. S3).

To determine which of the NAADP-sensitive channels may be involved in modulating the cellular alterations mediated by increased intracellular iron, we expressed tagged versions of the distinct channels, which were expressed to similar degrees and localized to endolysosomal structures, as previously described (Fig. S4).<sup>8</sup> Overexpression of either TPCN1 or TPCN2 increased the apoptosis induced by FAC or FeCl<sub>2</sub> treatment, which could be further potentiated by NAADP-AM (Fig. 8A, B; Fig. S5). In contrast, expression of channels containing mutations in a residue of the putative pore-forming helix<sup>53,54</sup> and shown to act as dominant-negative versions of either

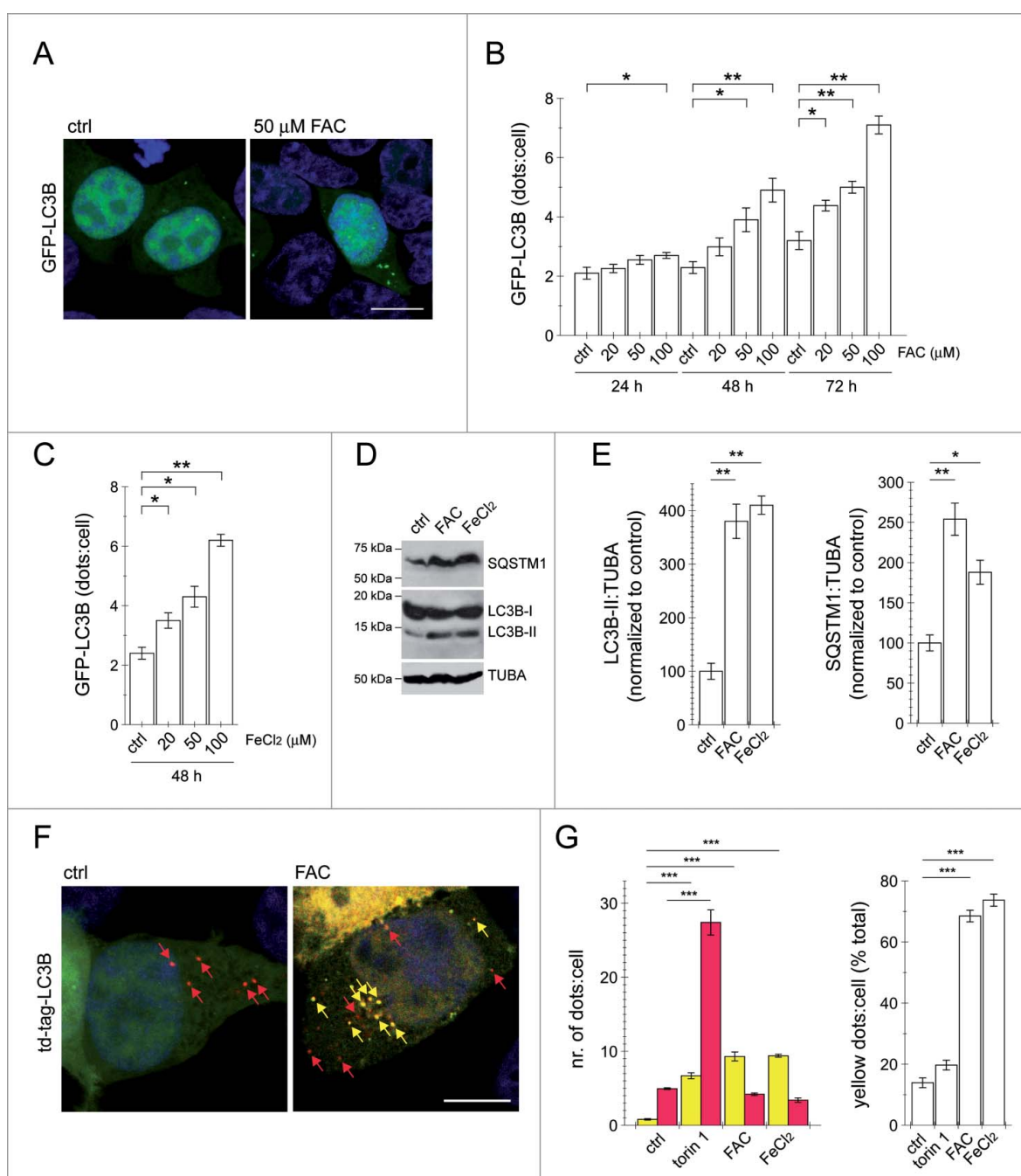


**Figure 3.** Iron overload impairs autophagic flux. (A) Representative examples of HEK293T cells transfected with GFP-LC3B either in the absence (ctrl) or presence of FAC for 48 h. Scale bar: 10  $\mu$ m. Quantification of the number of GFP-LC3B dots per cell in the absence (ctrl) or presence of the indicated amounts and times of FAC (B) or FeCl<sub>2</sub> application (C). Bars represent mean  $\pm$  SEM (n = 3; \*, P < 0.05; \*\*, P < 0.001). (D) Cells were either left untreated (ctrl) or treated as indicated, and extracts analyzed for endogenous LC3B-I/-II, SQSTM1 and TUBA. (E) Quantification of LC3B-II:TUBA or SQSTM1:TUBA from experiments of the type described in (D). Bars represent mean  $\pm$  SEM (n = 3; \*, P < 0.05; \*\*, P < 0.005). (F) Representative examples of HEK293T cells transfected with td-tag-LC3B either in the absence (ctrl) or presence of FAC for 48 h. Scale bar: 10  $\mu$ m. (G) Left: Quantification of the number of yellow and red td-tag-LC3B dots per cell either in the absence (ctrl) or presence of torin 1, FAC or FeCl<sub>2</sub> as indicated. Right: Quantification of the percentage of yellow td-tag-LC3B dots per cell either in the absence (ctrl) or presence of torin 1, FAC or FeCl<sub>2</sub> as indicated. Bars represent mean  $\pm$  SEM (n = 3; \*\*\*, P < 0.001).

TPCN1 (TPCN1<sup>L273P</sup>) or TPCN2 (TPCN2<sup>L265P</sup>) abolished the FAC or FeCl<sub>2</sub>-mediated increase in apoptosis observed with wild-type channels, and prevented the NAADP-mediated potentiation of cell death (Fig. 8A, B; Table 1). This was not due to differences in expression levels or aberrant subcellular localization, as both wild-type and mutant channels were expressed to similar degrees and properly localized to endolysosomal structures (Fig. S4). The effects of FAC or FeCl<sub>2</sub> in TPCN1- or TPCN2-expressing cells were abolished by Ned-19

(Fig. 8C, D; Fig. S5), suggesting that they were dependent on proper channel functioning and regulated in an NAADP-mediated manner. Thus, expression of active endolysosomal TPCN channels potentiates the deleterious effects of increasing intracellular iron content in a manner further potentiated by NAADP-AM and reversed by Ned-19.

MCOLN1 and MCOLN2 are permeable to iron,<sup>11</sup> but such iron permeability has not been investigated for TPCNs. Since MCOLN1 has been reported to form heterodimers with TPCN2,

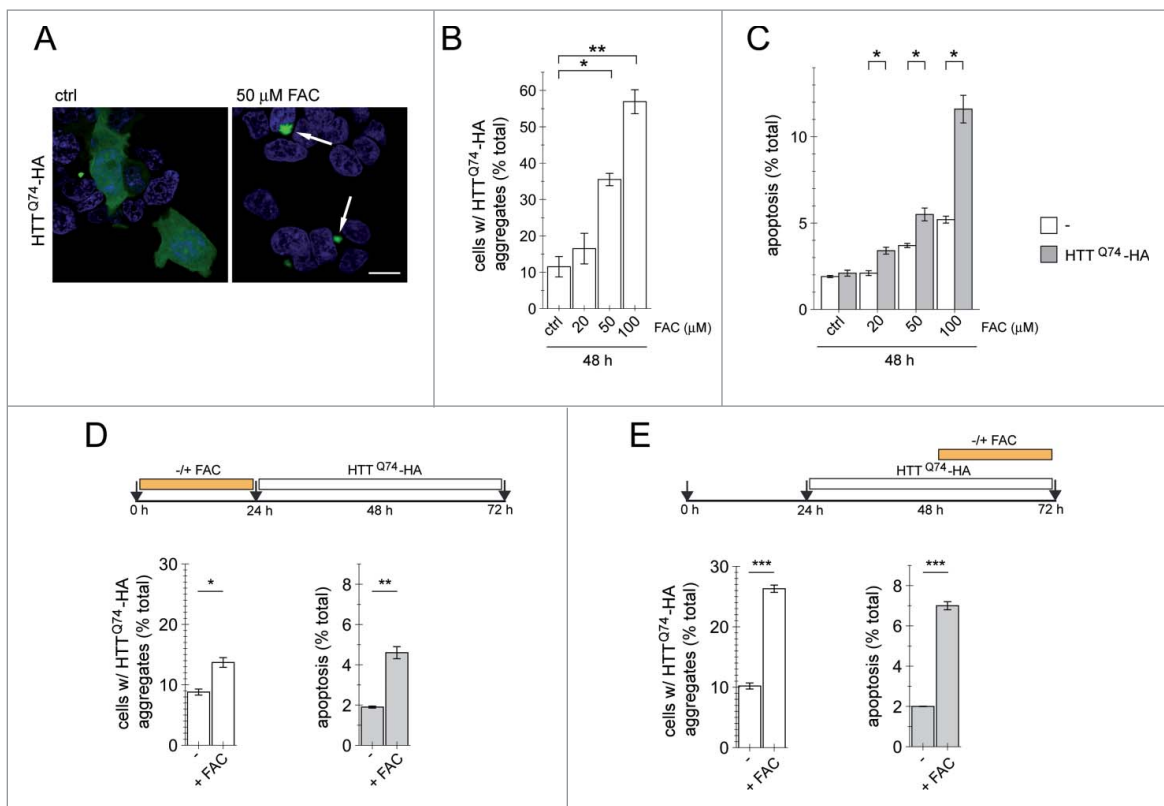


**Figure 4.** Increased intracellular iron causes deficits in clearance of aggregate-prone protein associated with increased cell death. (A) Representative examples of HEK293T cells transfected with HTT<sup>Q74</sup>-HA either in the absence (ctrl) or presence of FAC for 48 h. Arrows point to aggregates. Scale bar: 10  $\mu$ m. (B) Quantification of the percentage of cells displaying HTT<sup>Q74</sup>-HA aggregates in the absence (ctrl) or presence of the indicated amounts of FAC applied during 48 h. Bars represent mean  $\pm$  SEM (n = 3; \*, P < 0.005; \*\*, P < 0.001). (C) Quantification of the percentage of apoptosis in untransfected or HTT<sup>Q74</sup>-HA expressing cells either in the absence (ctrl) or presence of the indicated amounts of FAC applied during 48 h. Bars represent mean  $\pm$  SEM (n = 3; \*, P < 0.05). (D) Cells were pretreated in the presence or absence of 50  $\mu$ M FAC during 24 h before transfection as indicated, followed by quantification of the percentage of cells displaying aggregates (left) and apoptosis (right). Bars represent mean  $\pm$  SEM (n = 3; \*, P < 0.05; \*\*, P < 0.005). (E) Cells were transfected as indicated, and either left untreated, or treated with 50  $\mu$ M FAC during the last 24 h as indicated, followed by quantification of the percentage of cells displaying aggregates (left) and apoptosis (right). Bars represent mean  $\pm$  SEM (n = 3; \*\*\*, P < 0.001).

and to a lesser degree with TPCN1,<sup>55</sup> we wondered whether the observed iron-mediated effects of the TPCNs may be due to their heterogeneous interactions with MCOLN1 channels. Expression of TPCN2 caused an increase in FAC-mediated apoptosis which was abolished when coexpressing the TPCN2 pore mutant (Fig. 9). Similarly, expression of MCOLN1 caused an increase in FAC-mediated apoptosis abolished when coexpressing a MCOLN1 mutant (MCOLN1<sup>T232P</sup>) defective in iron conductance (Fig. 9, Table 1).<sup>11</sup> Coexpression of TPCN2 with MCOLN1 caused an additive increase in FAC-mediated apoptosis. However, coexpression of mutant MCOLN1<sup>T232P</sup> along with TPCN2 did not abolish the TPCN2-mediated increase in cell death in the presence of FAC. Similarly, coexpression of mutant TPCN2 did not abolish the MCOLN1-mediated increase in cell death in the presence of FAC (Fig. 9). Therefore, TPCN and MCOLN channels seem to function independently from each other in mediating the cellular effects of increased intracellular iron.

To further probe the role of TPCNs, we performed shRNA experiments.<sup>53,56</sup> Silencing of both TPCN1 and TPCN2 increased apoptosis under basal conditions, and also increased apoptosis upon FAC treatment, suggesting that TPCN channels may be important for cell survival under our cell culture conditions (Fig. S6). Notably, and in contrast to untransfected cells, cell death in knockdown cells was not further modulated by either NAADP-AM or Ned-19 (Fig. S6), indicating that the modulation of iron-

mediated cell death by NAADP-AM and Ned-19 as reported here is largely mediated by TPCN channels.

### NAADP and TPCN channels regulate endolysosomal and cytosolic iron levels

Increased intraorganellar iron load may be responsible for the observed effects of FAC treatment on endolysosomal structure and functioning, and modulation of TPCN channels may cause endolysosomal iron release, followed by increased cytosolic oxidative stress and eventual cell death. To demonstrate iron accumulation in endolysosomes, we stained for endolysosomal iron using the sulphide-silver method.<sup>11,57</sup> Cells were either left untreated, treated with FAC or FeCl<sub>2</sub>, or treated with Fe<sup>3+</sup>-dextran, which is endocytosed and exclusively accumulates in endolysosomes.<sup>11</sup> As previously described, Fe<sup>3+</sup>-dextran-loaded cells displayed significantly more iron staining as compared to control cells, which often localized to the vicinity of the nucleus, typical for the intracellular positioning of endolysosomes (Fig. 10A). Similarly, FAC or FeCl<sub>2</sub>-treated cells displayed a significant increase in iron staining as compared to control cells, which was mostly localized to a perinuclear area (Fig. 10A, B). Cells expressing TPCN1 or TPCN2 displayed a further FAC or FeCl<sub>2</sub>-mediated increase in iron staining, and such increased staining was largely abolished when treating cells with NAADP-AM, but not Ned-19 (Fig. 10C, D).

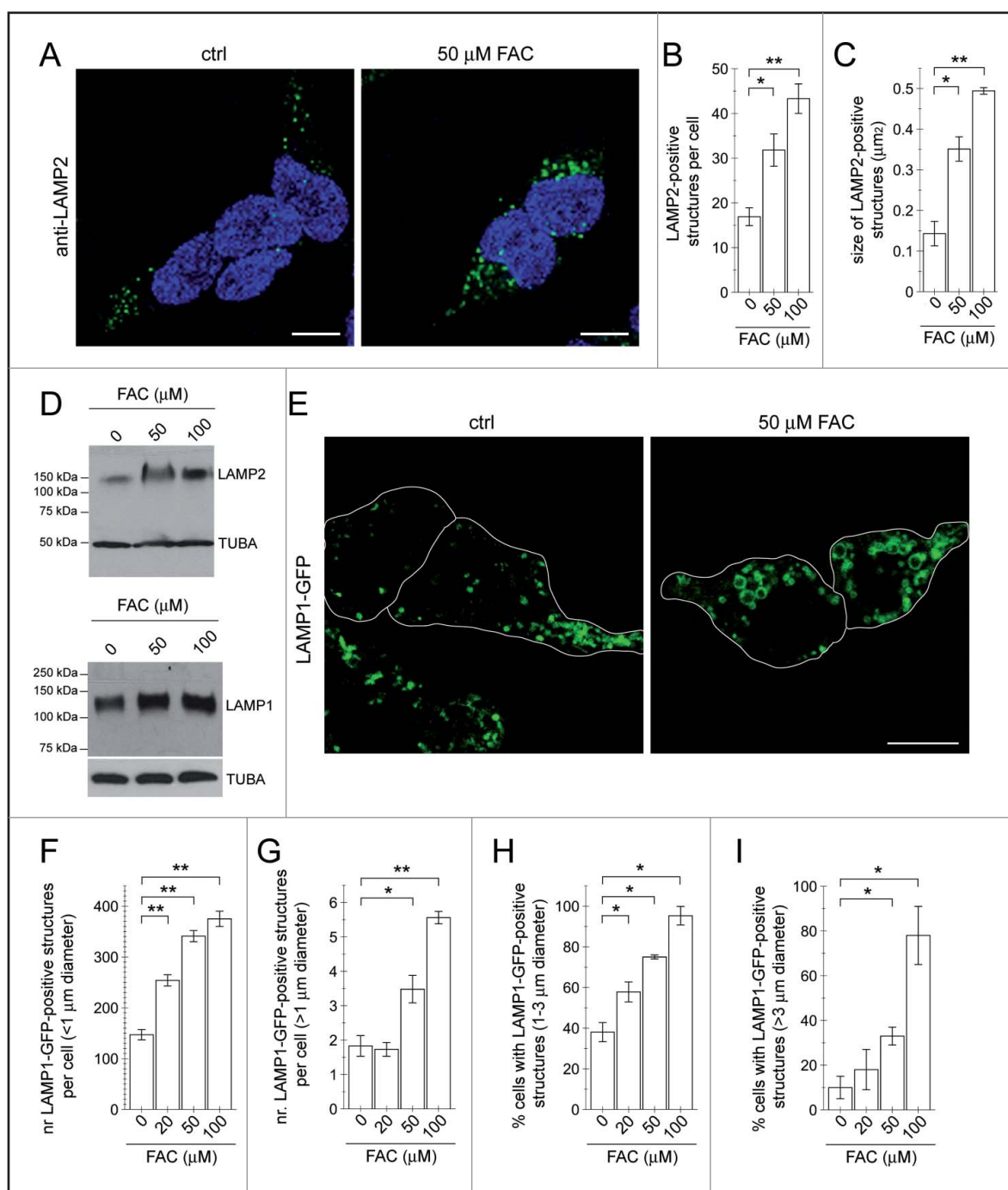


**Figure 5.** Increasing intracellular iron causes endolysosomal alterations. (A) Representative images of HEK293T cells stained with LAMP2 either in the absence (ctrl) or presence of FAC incubation for 48 h. Scale bar: 10  $\mu\text{m}$ . (B) Quantification of the number of LAMP2-positive structures per cell in the absence or presence of FAC treatment. Bars represent mean  $\pm$  SEM ( $n = 3$ ; \*,  $P < 0.05$ ; \*\*,  $P < 0.005$ ). (C) Quantification of the size of LAMP2-positive structures in the absence or presence of the indicated concentrations of FAC. Bars represent mean  $\pm$  SEM ( $n = 3$ ; \*,  $P < 0.05$ ; \*\*,  $P < 0.005$ ). (D) Cells were treated with FAC for 48 h, and extracts analyzed for levels of LAMP2 (top) or LAMP1 (bottom), with TUBA as loading control. (E) Representative images of live HEK293T cells transfected with LAMP1-GFP and either left untreated (ctrl) or incubated with FAC for 48 h. Scale bar: 10  $\mu\text{m}$ . (F) Quantification of the number of LAMP1-GFP-positive structures per cell equal or smaller than 1  $\mu\text{m}$  in diameter, in the absence or presence of the indicated concentrations of FAC for 48 h. Bars represent mean  $\pm$  SEM ( $n = 3$ ; \*\*,  $P < 0.005$ ). (G) Quantification of the number of LAMP1-GFP-positive structures per cell bigger than 1  $\mu\text{m}$  in diameter, in the absence or presence of the indicated concentrations of FAC for 48 h. Bars represent mean  $\pm$  SEM ( $n = 3$ ; \*,  $P < 0.05$ ; \*\*,  $P < 0.001$ ). (H) Quantification of the percentage of transfected cells with at least one LAMP1-GFP-positive structure with a diameter of between 1 to 3  $\mu\text{m}$ . Bars represent mean  $\pm$  SEM ( $n = 3$ ; \*,  $P < 0.05$ ). (I) Quantification of the percentage of transfected cells with at least one LAMP1-GFP-positive structure with a diameter larger than 3  $\mu\text{m}$ . Bars represent mean  $\pm$  SEM ( $n = 3$ ; \*,  $P < 0.05$ ).

Moreover, no NAADP-AM-mediated alterations in iron staining were observed in cells expressing mutant TPCN1 or TPCN2, consistent with those mutants acting as dominant-negative pore mutants (Fig. 10E, F).

We next measured the levels of free (chelatable) cytosolic iron levels upon modulation of TPCN channels using a fluorescence-based iron dequenching imaging method.<sup>11</sup> FAC treatment caused an increase in cytosolic iron which was

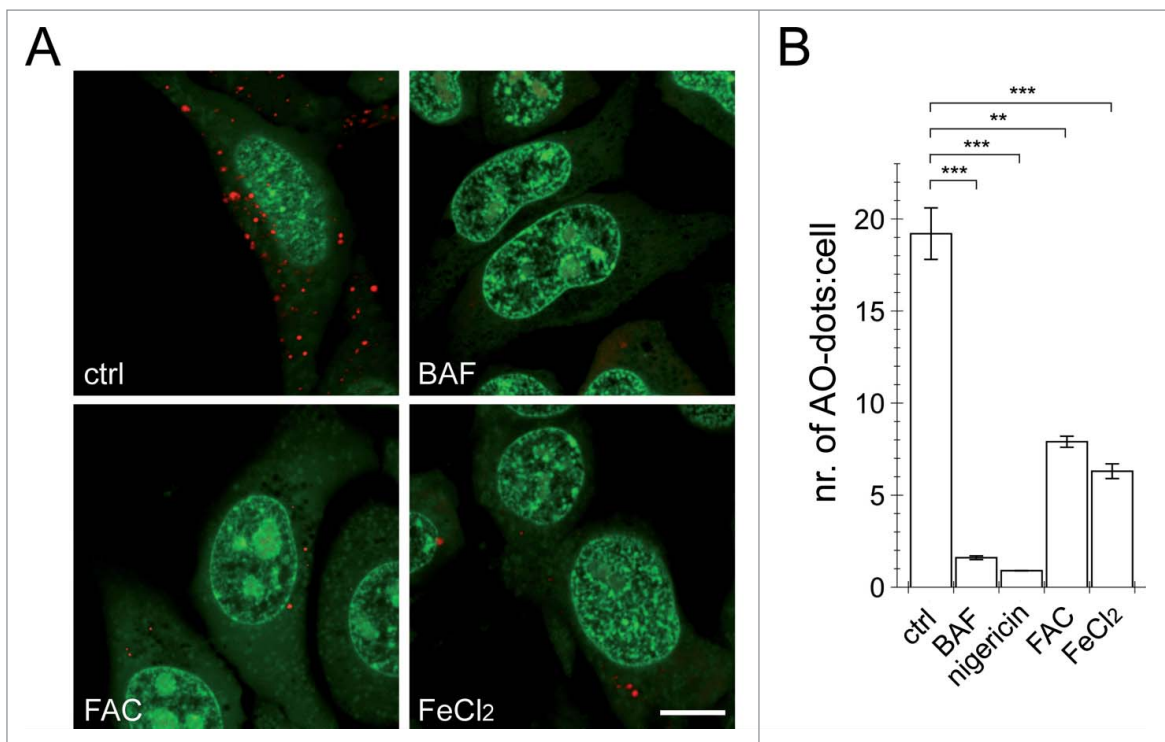


**Figure 6.** Increasing intracellular iron causes alterations in endolysosomal pH. (A) Representative images of live HEK293T cells either left untreated (ctrl), or treated with BAF, FAC or FeCl<sub>2</sub> as indicated, followed by staining with acridine orange. Scale bar: 10  $\mu$ m. (B) Quantification of the number of acridine orange-positive structures per cell in the absence (ctrl) or presence of treatments as indicated. Bars represent mean  $\pm$  SEM (n = 3; \*\*,  $P < 0.005$ ; \*\*\*,  $P < 0.001$ ).

potentiated by NAADP-AM and sensitive to the NAADP antagonist Ned-19 (Fig. 11A, B). In cells expressing wild-type but not mutant TPCN2, FAC treatment further increased cytosolic iron levels in a manner sensitive to NAADP-AM and reverted by Ned-19 (Fig. 11C, D). Identical findings were observed in cells expressing TPCN1, but not mutant TPCN1 (Fig. 11E). Altogether, these data indicate that iron accumulates in endolysosomal compartments, and that both endolysosomal TPCN channels can regulate cytosolic iron homeostasis subject to modulation by NAADP-AM and Ned-19.

#### Iron-mediated cytotoxicity is regulated by RAB7A activity

Apart from NAADP, TPCN channels have been reported to be modulated by the small GTPase RAB7A.<sup>22</sup> Thus, we next wondered whether the enhanced FAC-mediated apoptosis in TPCN-expressing cells may be regulated by the coexpression of various RAB7A constructs. Whereas coexpression of wild-type RAB7A was without effect, the constitutively active, GTP-locked RAB7A<sup>Q67L</sup> mutant further enhanced the FAC-mediated increase in apoptosis observed upon TPCN2 expression (Fig. 12A, Table 1). Interestingly, coexpression of the dominant-negative, GTP binding-defective RAB7A<sup>T22N</sup> mutant fully abolished the effects of TPCN2 on enhancing apoptosis in the presence of increased iron load (Fig. 12A), and this could not be modulated by NAADP-AM (Fig. 12B). Conversely, Ned-19 abolished the effects of TPCN2 expression on FAC-mediated apoptosis irrespective of the presence of the various RAB7A constructs (Fig. 12C). These data suggest that RAB7A may act downstream from NAADP to regulate TPCN2 activity.

The enhancement of FAC-mediated apoptosis in the presence of constitutively active RAB7A was not observed in cells coexpressing TPCN1, but enhanced cell death in the presence of FAC in TPCN1-expressing cells was also blocked when coexpressing dominant-negative RAB7A (Fig. 12D). Together, these data suggest that the behavior of TPCN channels are modulated by dominant-negative RAB7A, whereas constitutively active, GTP-locked RAB7A only potentiates the effects of TPCN2.

Further evidence for the RAB7A-mediated regulation of TPCN2 activity in the context of cell death induced by iron overload was obtained by overexpressing a triple mutant TPCN2 version (TPCN2[3A]; Q33A,V34A,P36A) previously shown to display drastically reduced binding to RAB7A (Table 1).<sup>22</sup> This mutant increased FAC-mediated apoptosis to a comparable degree as wild-type TPCN2, and in contrast to the dominant-negative, inactive TPCN2 pore mutant (Fig. 13A). However, the effects of FAC on apoptosis in the presence of TPCN2[3A] were not further potentiated by catalytically active RAB7A (Fig. 13B).

Finally, a pharmacological RAB inhibitor<sup>58</sup> (CID1067700) reverted the FAC-induced apoptosis in the presence of TPCN2, as well as in the presence of TPCN2 and either wild-type or constitutively active RAB7A (Fig. 13C). As CID1067700 has been reported to compete with the GTP binding capacity of RAB7A,<sup>58</sup> these data support the notion that the potentiating effect of the RAB7A<sup>Q67L</sup> mutant is indeed due to enhanced activity (Fig. 13C). Together, these data indicate that TPCN channels mediate release of iron from acidic stores, and that their function can be modulated by altering the GTPase activity of RAB7A.

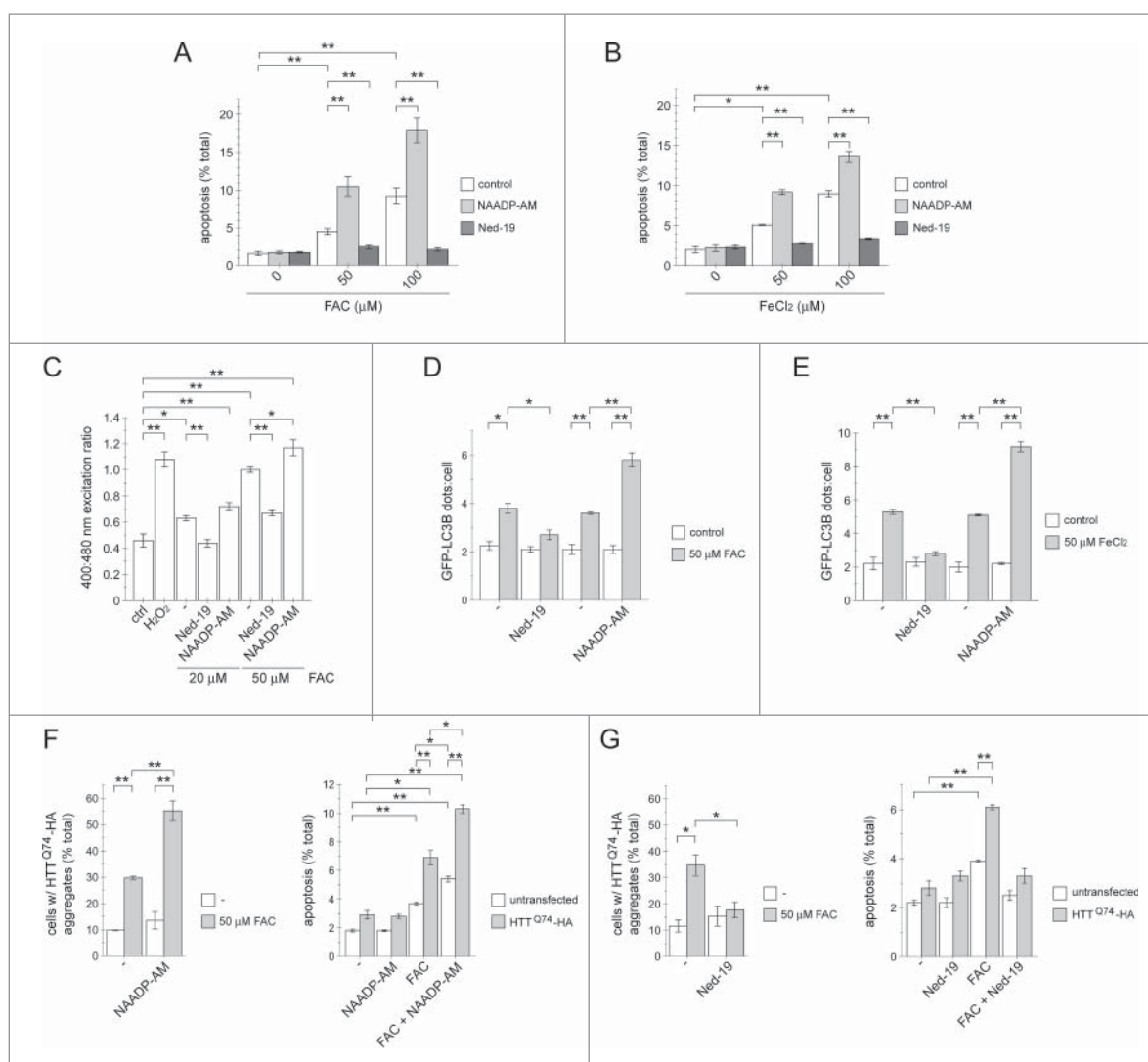


**Figure 7.** NAADP-mediated modulation of effects associated with increased iron load. Dose-dependent increase in FAC-mediated (A) or FeCl<sub>2</sub>-mediated (B) apoptosis in HEK293T cells is potentiated upon 12 h incubation with 100 nM NAADP-AM, and abolished upon 12 h incubation with 1  $\mu$ M Ned-19. Graphs represent mean  $\pm$  SEM (n = 3; \*,  $P < 0.05$ ; \*\*,  $P < 0.005$ ). (C) Quantification of oxidation induced by either hydrogen peroxide or increasing concentrations of FAC (48 h) in the absence or presence of NAADP-AM or Ned-19, respectively. NAADP-AM slightly potentiates, and Ned-19 potently inhibits FAC-mediated oxidation. Bars represent mean  $\pm$  SEM (n = 3; \*,  $P < 0.05$ , \*\*,  $P < 0.005$ ). FAC-mediated (D) or FeCl<sub>2</sub>-mediated (E) increase in autophagosome numbers is potentiated by NAADP-AM and reverted by Ned-19. Quantification of the number of GFP-LC3B dots per cell in the absence or presence of FAC, and in the absence or presence of NAADP-AM or Ned-19, respectively. Bars represent mean  $\pm$  SEM (n = 3; \*,  $P < 0.05$ ; \*\*,  $P < 0.005$ ). (F) Quantification of the percentage of cells displaying HTT<sup>Q74</sup>-HA aggregates (left) or apoptosis (right) in the absence or presence of FAC, and in the absence or presence of NAADP-AM. Bars represent mean  $\pm$  SEM (n = 3; \*,  $P < 0.05$ ; \*\*,  $P < 0.005$ ). (G) Quantification of the percentage of cells displaying HTT<sup>Q74</sup>-HA aggregates (left) or apoptosis (right) in the absence or presence of FAC, and in the absence or presence of Ned-19. Bars represent mean  $\pm$  SEM (n = 3; \*,  $P < 0.05$ ; \*\*,  $P < 0.005$ ).

## Discussion

The present study shows for the first time that increased endolysosomal iron load causes deficits in the proper structure and function of these organelles, increased cytosolic oxidative stress and eventual cell death. These events are associated with increased autophagy initiation but impaired autophagic completion, as indicated by the decreased clearance of protein aggregates. The observed effects are potentiated by NAADP-AM and reverted by Ned-19, implicating a role for endolysosomal NAADP-sensitive cation channels. Indeed, overexpression of active but not inactive TPCN channels aggravates iron-induced cell death in a manner sensitive to NAADP-AM and Ned-19. Moreover, both endolysosomal iron staining and iron-sensitive fluorescence imaging indicate that TPCN channels mediate endolysosomal iron release in a

manner modulated by NAADP-AM. The iron-mediated effects on cell death are also shown to be regulated by the activity of RAB7A, a regulator of endolysosomal and autophagic trafficking steps. Together, these studies highlight novel approaches which may have beneficial effects in treating diverse disorders associated with altered iron handling. Interestingly, modulating TPCN channels and RAB7A activity have also recently been shown to revert various cellular deficits related to pathogenic LRRK2, mutations which cause Parkinson disease,<sup>59,60</sup> indicating that they may comprise more general therapeutic targets for neurodegenerative disorders beyond iron dyshomeostasis.

Increased brain iron has been associated with several sporadic and genetic disorders manifesting as movement disorders.<sup>2</sup> Since increased iron content may secondarily contribute to the disease process, strategies to modulate intracellular iron handling may

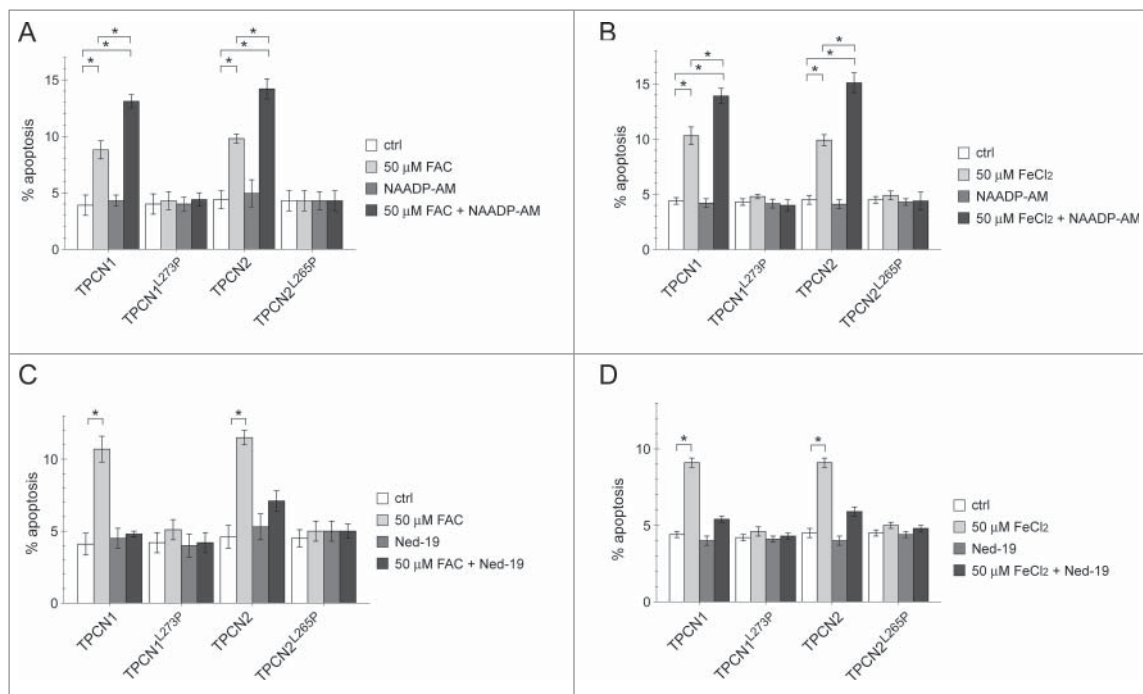


**Figure 8.** Expression of TPCN channels potentiates FAC-mediated cell death in a NAADP- and Ned-19-sensitive manner. Quantification of apoptosis mediated by FAC (A) or FeCl<sub>2</sub> (B) in HEK293T cells expressing either wild-type or dominant-negative TPCN1 or TPCN2 channels, respectively, in either the absence or presence of 100 nM NAADP-AM. Bars represent mean  $\pm$  SEM ( $n = 3$ ; \*,  $P < 0.05$ ). Quantification of apoptosis mediated by FAC (C) or FeCl<sub>2</sub> (D) in cells expressing either wild-type or dominant-negative TPCN1 or TPCN2 channels, respectively, in either the absence or presence of 1  $\mu$ M Ned-19. Bars represent mean  $\pm$  SEM ( $n = 3$ ; \*,  $P < 0.05$ ).

prove beneficial. However, this requires a better understanding of the mechanisms and molecular players regulating intracellular iron handling. Our current data suggest various possible targets including NAADP-sensitive endolysosomal cation channels and RAB7A activity.

Lysosomes have emerged as important mediators of metal homeostasis.<sup>4</sup> Indeed, our iron imaging data indicate that a significant amount of iron can be stored in endolysosomal organelles. Increased iron content seems associated with lysosomal proliferation, an enlargement of endolysosomal structures, an increase in endolysosomal pH and a deficit in autophagic flux. It remains possible that an alteration in the relative ion fluxes through the various endolysosomal cation channels may cause the observed deficits in proper late endocytic and autophagic trafficking and endolysosomal size via altered fusion and fission of late endosomes and lysosomes.<sup>61</sup> However, application of BAPTA-AM, which chelates both calcium as well as iron, reverted the NAADP-mediated increase in cell death in TPCN-transfected cells (Fig. S7), which at least excludes altered sodium fluxes through TPCN channels<sup>9,10</sup> as being implicated in the observed effects. In addition, the involvement of impaired iron homeostasis is further supported by

previous observations that increased levels of intralysosomal iron induce an enlargement of lysosomes and an overall increase in intralysosomal pH.<sup>11,62</sup>

The observed increase in cytosolic oxidative stress upon iron load was found to be modulated by NAADP-AM and Ned-19, indicating the involvement of endolysosomal NAADP-sensitive channels in controlling cytosolic prooxidant iron levels. The specific NAADP-mediated modulation suggests that alterations in oxidative stress are not merely a consequence of lysosomal rupture or altered lysosomal membrane permeability. In agreement with this, the NAADP antagonist Ned-19 reverted the observed

**Table 1.** Summary of the different mutant versions of TPCN1, TPCN2, MCOLN1 and RAB7A constructs used in the present study and their functional consequences.

Mutant	Molecular purpose
TPCN1 <sup>L273P</sup>	pore mutant, dominant-negative
TPCN2 <sup>L265P</sup>	pore mutant, dominant-negative
TPCN2[3A]	defective in binding to RAB7A
MCOLN1 <sup>T232P</sup>	defective in iron conductance
RAB7A <sup>Q67L</sup>	constitutively active, GTP locked
RAB7A <sup>T22N</sup>	dominant-negative, GTP binding-deficient

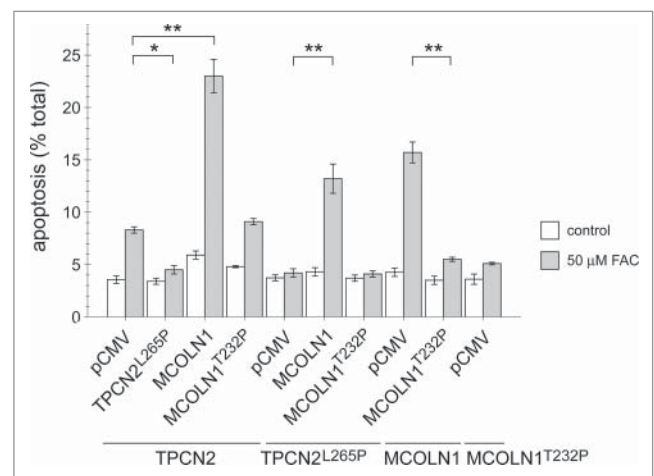


**Figure 9.** TPCN2 and MCOLN1 function independently from each other to mediate iron-induced cytotoxicity. Cells were cotransfected with the indicated constructs, and cell death analyzed in either the absence or presence of 50  $\mu$ M FAC for 48 h. Bars represent mean  $\pm$  SEM ( $n = 3$ ; \*,  $P < 0.05$ ; \*\*,  $P < 0.005$ ).

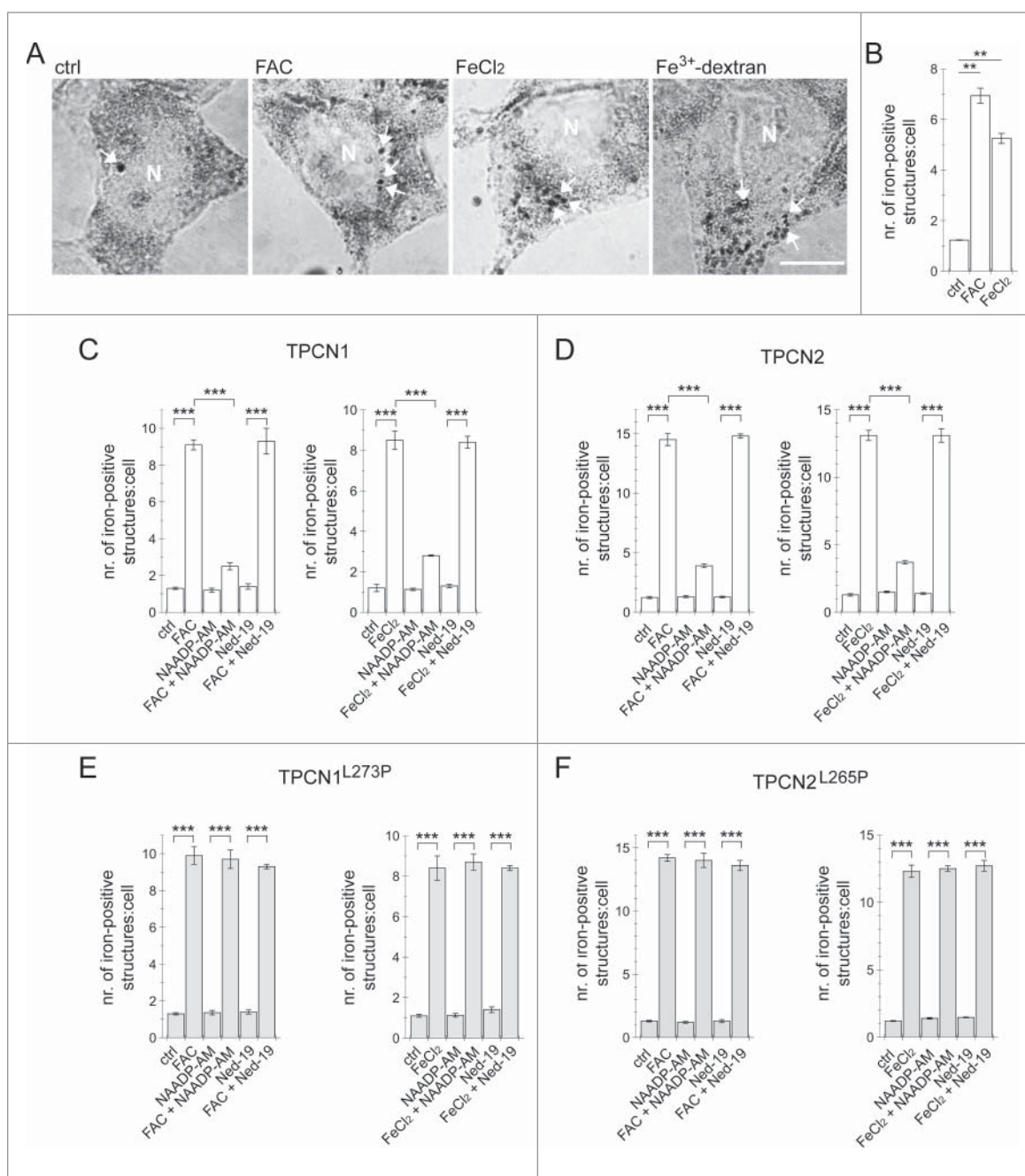


**Figure 10.** NAADP-mediated alterations in endolysosomal iron levels in control and TPCN-expressing cells. (A) Representative images of HEK293T cells either left untreated (ctrl), treated with FAC, FeCl<sub>2</sub> or Fe<sup>3+</sup>-dextran as indicated, and stained for intracellular iron using the sulphide-silver method. Scale bar: 10  $\mu$ m. (B) Quantification of the number of iron-positive structures per cell in the absence (ctrl) or presence of 48 h treatment with 50  $\mu$ M FAC or 50  $\mu$ M FeCl<sub>2</sub> as indicated. Bars represent mean  $\pm$  SEM (n = 3; \*\*,  $P < 0.005$ ). Quantification of the number of iron-positive structures in cells expressing TPCN1 (C) or TPCN2 (D) in the absence (ctrl) or presence of 48 h treatment with 50  $\mu$ M FAC or 50  $\mu$ M FeCl<sub>2</sub>, respectively, and in the presence or absence of 100 nM NAADP-AM or 1  $\mu$ M Ned-19 for the last 12 h as indicated. Bars represent mean  $\pm$  SEM (n = 3; \*\*\*,  $P < 0.001$ ). Quantification of the number of iron-positive structures in cells expressing dominant-negative mutants of TPCN1 (E) or TPCN2 (F) in the absence (ctrl) or presence of 48 h treatment with 50  $\mu$ M FAC or 50  $\mu$ M FeCl<sub>2</sub>, respectively, and in the presence or absence of 100 nM NAADP-AM or 1  $\mu$ M Ned-19 for the last 12 h as indicated. Bars represent mean  $\pm$  SEM (n = 3; \*\*\*,  $P < 0.001$ ).

iron-mediated increase in oxidative stress, autophagosome numbers, deficits in autophagic protein aggregate clearance and structural endolysosomal alterations. It remains unclear whether autophagy induction is a consequence of increased cytosolic oxidant stress<sup>39</sup> or a result of the impairment of trafficking and degradative capacity along the late endolysosomal pathway, but it is reasonable to assume that both processes contribute to the alterations observed here.

Endolysosomes seem to function as iron storage organelles conferring at least partial protection from cell death in the context of iron overload, as evidenced by the observation that inducing endolysosomal iron efflux causes increased cytoplasmic oxidative stress and enhanced cytotoxicity. At the same time, increased endolysosomal iron also interferes with proper autophagic clearance. Whereas this does not seem to alter cell survival under basal conditions, it becomes detrimental to cell

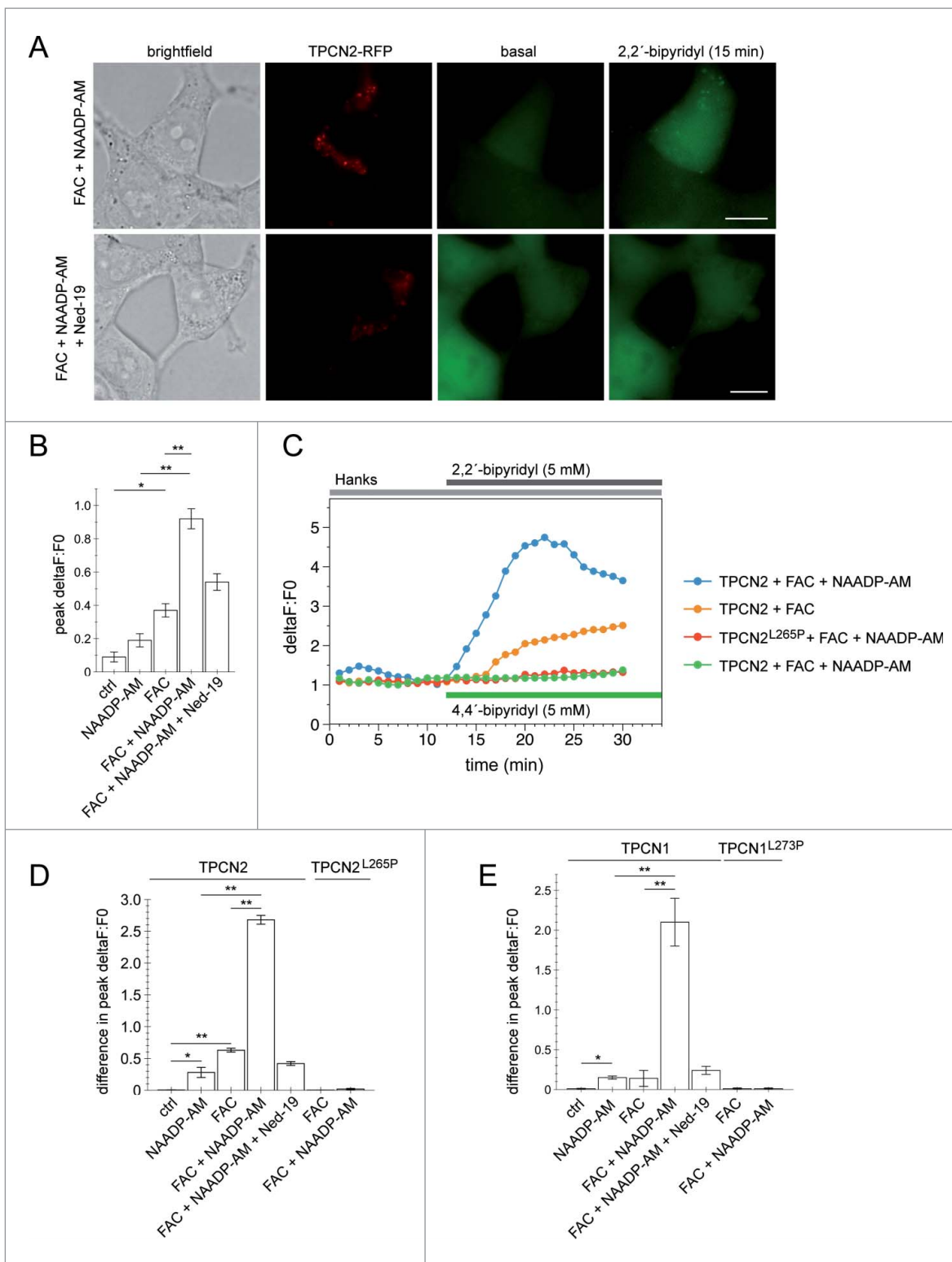


**Figure 11.** TPCN channel-expressing cells have increased free iron levels modulated in an NAADP-mediated fashion. (A) Representative examples of dequenching of TPCN2-RFP-transfected HEK293T cells upon incubation with FAC and either 100 nM NAADP-AM (top row), or 100 nM NAADP-AM and 1  $\mu$ M Ned-19 (bottom row). Transfected cells show more dequenching of the iron-sensitive fluorescence as compared to untransfected cells, and dequenching is abolished in the presence of 1  $\mu$ M Ned-19. Dequenching was achieved by preloading the cells with an iron-sensitive dye (Phen Green SK), followed by addition of the membrane-permeable transition metal chelator, 2,2'-bipyridyl, which chelates free cellular iron, causing a concomitant increase in Phen Green SK fluorescence. Scale bar: 10  $\mu$ m. (B) Quantification of the 2,2'-bipyridyl-induced normalized change of peak fluorescence (peak  $\Delta F:F0$ ) in the absence or presence of FAC, NAADP-AM or Ned-19 as indicated. Bars represent mean  $\pm$  SEM ( $n = 3$ ; \*,  $P < 0.05$ ; \*\*,  $P < 0.005$ ). (C) Example of 2,2'-bipyridyl-induced normalized changes in fluorescence ( $\Delta F:F0$ ) in either wild-type or mutant TPCN2-expressing cells (average of 30 to 40 cells each) in the presence of FAC and NAADP-AM as indicated. Green trace indicates absence of fluorescence dequenching upon addition of 4,4'-bipyridyl, a 2,2'-bipyridyl analog which cannot bind iron. (D) Quantification of the 2,2'-bipyridyl-induced normalized change of peak fluorescence (peak  $\Delta F:F0$ ) in either wild-type or mutant TPCN2-expressing cells, in the absence or presence of FAC, NAADP-AM or Ned-19 as indicated. Bars represent mean  $\pm$  SEM ( $n = 3$ ; \*,  $P < 0.05$ ; \*\*,  $P < 0.005$ ). (E) Quantification of iron dequenching as described above in either wild-type or mutant TPCN1-expressing cells. Bars represent mean  $\pm$  SEM ( $n = 3$ ; \*,  $P < 0.05$ ).

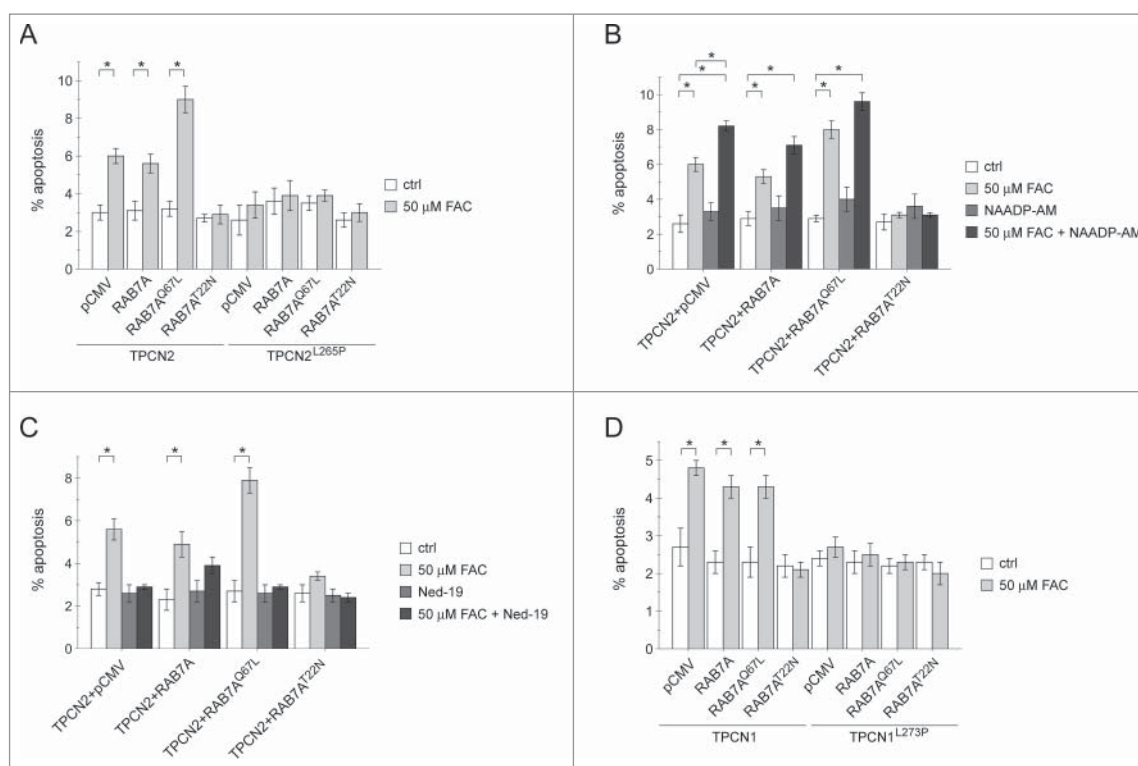


**Figure 12.** RAB7A expression modulates iron-mediated cytotoxicity in TPCN-channel-expressing cells. (A) Quantification of apoptosis in HEK293T cells coexpressing either wild-type or mutant TPCN2, and either empty control vector (pCMV), RAB7A, GTP-locked RAB7A<sup>O67L</sup> or GTP binding-defective RAB7A<sup>T22N</sup>, respectively, in the absence or presence of FAC. Bars represent mean  $\pm$  SEM (n = 3; \*, P < 0.05). (B) Quantification of apoptosis in cells coexpressing the indicated constructs, and either in the absence or presence of FAC and NAADP-AM as indicated. Bars represent mean  $\pm$  SEM (n = 3; \*, P < 0.05). (C) Quantification of apoptosis in cells coexpressing the indicated constructs, and either in the absence or presence of FAC and Ned-19 as indicated. Bars represent mean  $\pm$  SEM (n = 3; \*, P < 0.05). (D) Quantification of apoptosis in the absence or presence of FAC in cells coexpressing either wild-type or mutant TPCN1, and either empty vector or various RAB7A constructs as described above. Bars represent mean  $\pm$  SEM (n = 3; \*, P < 0.05).

survival under conditions which require enhanced autophagic flux, as evidenced by the finding that expression of aggregate-prone HTT<sup>Q74</sup> protein causes an increase in apoptosis in the presence of FAC. Thus, endolysosomal iron storage may act as a “double-edged sword” for cell survival. It may play a cytoprotective role under basal conditions which do not require autophagic activity, while becoming a liability issue under cellular conditions requiring productive autophagy for cell survival, such as protein aggregation-induced stress.

Iron overload was found to enhance protein aggregation and cell death both when occurring before protein aggregation was triggered, as well as when aggregation was already existent. Whereas these data do not allow to draw conclusions as to which event comes first, they are consistent with *in vivo* data reporting damaging effects of neonatal iron supplementation on neurodegeneration in a mouse model of Huntington disease, and with the reported beneficial effects of an iron chelator on motor phenotypes in adult mice of the same mouse model.<sup>63,64</sup>

The primary pathway for cellular iron uptake occurs via receptor-mediated endocytosis of iron-bound transferrin, reduction of iron, and subsequent release from late endosomes and lysosomes into the cytosol.<sup>32–34</sup> Once in the cytosol, iron enters the labile iron pool and is stored in ferritin, from which it can be mobilized again as needed via autophagy-dependent and -independent processes,<sup>65–67</sup> ending with the lysosomal degradation of ferritin-iron complexes and subsequent transport of reduced iron into the cytosol. Thus, both extracellular iron uptake and intracellular iron mobilization require transport of reduced iron across the

endolysosomal membrane. A variety of transporters have been described to serve this role, including DMT1, NRAMP1 and MCOLN channels.<sup>11,68</sup> TPCN channels are ubiquitously expressed, are permeable to various ions including calcium and sodium<sup>7,9,10</sup> and are localized to endolysosomal structures. Over-expressed TPCN and MCOLN channels are exclusively localized to endolysosomal structures as well, since their expression is not associated with altered whole-cell currents,<sup>54,55</sup> excluding the possibility that they are mistargeted to the plasma membrane to cause an inward influx of iron from the extracellular medium. Thus, our current data indicate that TPCN channels also mediate iron release from endolysosomal organelles, adding to the list of endolysosomal iron-conducting channels. This feature of TPCN channels is not due to heterodimerization with the iron-conducting MCOLN channels,<sup>55</sup> and it depends on proper channel functioning, as not observed with the nonconducting TPCN pore-mutants. Therefore, both MCOLN and TPCN channels seem able to independently control iron homeostasis in endolysosomal organelles.

The iron-mediated effects observed here were potentiated by NAADP-AM and blocked by Ned-19, a highly specific NAADP antagonist.<sup>28</sup> TPCN channels are crucial for NAADP-mediated calcium release from endolysosomal stores,<sup>14–17</sup> and our present data indicate that TPCN-mediated endolysosomal iron release is also modulated by NAADP-AM and Ned-19. Ned-19 was without effect on apoptosis, oxidative stress, autophagosome accumulation, HTT<sup>Q74</sup> aggregation or endolysosomal iron accumulation on its own, but was able to revert all of the above-mentioned FAC-mediated alterations. Moreover, Ned-19 was able to revert the effects of

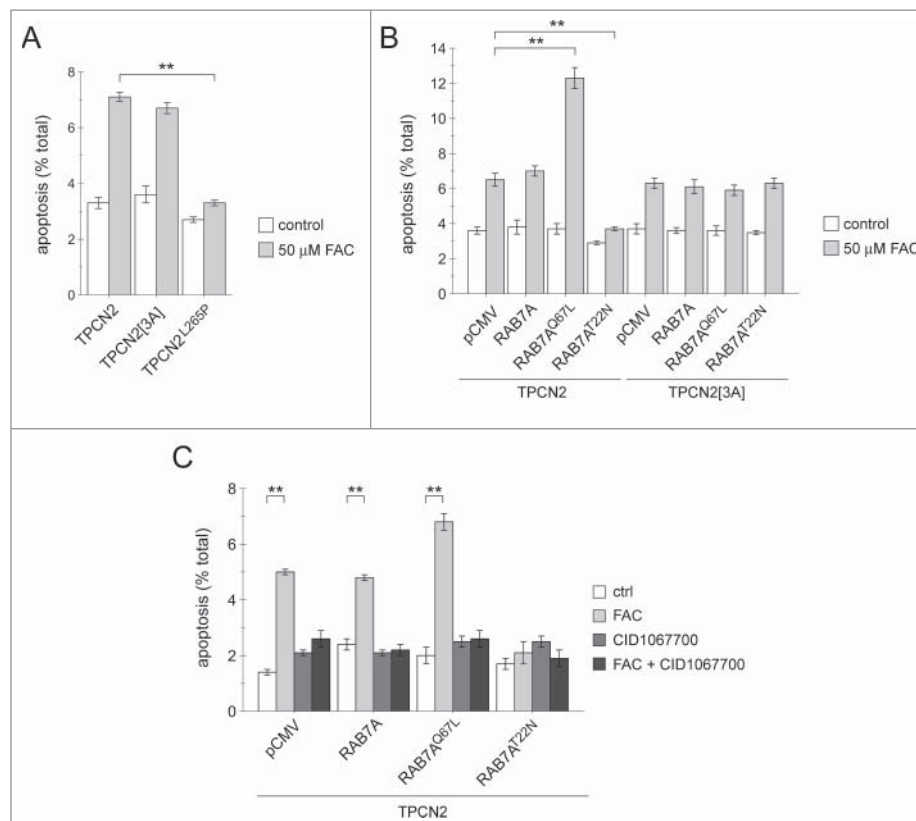


**Figure 13.** TPCN2-mediated modulation of iron-induced cytotoxicity is dependent on RAB7A activity. (A) Quantification of apoptosis in HEK293T cells expressing TPCN2, a TPCN2 mutant defective in RAB7A binding (TPCN2[3A]) or a dominant-negative pore mutant (TPCN2<sup>L265P</sup>), in the absence or presence of FAC, respectively. Bars represent mean  $\pm$  SEM ( $n = 3$ ; \*\*,  $P < 0.005$ ). (B) Quantification of apoptosis in cells coexpressing wild-type or RAB7A binding-deficient TPCN2 (TPCN2[3A]) and either empty vector (pCMV), wild-type RAB7A, GTP-locked RAB7A (RAB7A<sup>Q67L</sup>) or GTP binding-defective RAB7A (RAB7A<sup>T22N</sup>) in the absence or presence of FAC. Bars represent mean  $\pm$  SEM ( $n = 3$ ; \*\*,  $P < 0.005$ ). (C) Quantification of apoptosis in cells cotransfected with TPCN2 and either empty vector (pCMV), or various RAB7A constructs as indicated, in the absence or presence of FAC and 5  $\mu$ M CID1067700 for 4 h as indicated. Bars represent mean  $\pm$  SEM ( $n = 3$ ; \*\*,  $P < 0.005$ ).

NAADP-AM on increasing cytosolic iron, confirming its exquisite specificity as an NAADP antagonist. Finally, the iron-mediated apoptosis in TPCN knockdown cells was not further modulated by NAADP-AM or Ned-19. Therefore, even though it is likely that additional endolysosomal channels such as DMT1, NRAMP1 and MCOLN can contribute to iron efflux from endolysosomes, the modulation by NAADP-AM and Ned-19 as reported here is mediated via TPCN channels. While the precise molecular binding partner(s) for NAADP and Ned-19 remain to be identified,<sup>18,19</sup> this suggests that NAADP antagonists may prove beneficial in reverting endolysosomal iron dyshomeostasis associated with enhanced cytotoxicity.

The effects of increased intracellular iron on cell death were also modulated by RAB7A activity, with a GTP-locked mutant version of RAB7A enhancing cell death in TPCN2-expressing cells, but not in cells expressing TPCN1. As both TPCN1 and TPCN2 channels were expressed to similar degrees, the observed differential effects of active RAB7A on FAC-mediated apoptosis may be explained either by subtle differences in the subcellular localization of TPCN1 and TPCN2 along the endocytic pathway with respect to RAB7A,<sup>69,70</sup> or to differences in the affinity by which the 2 channels interact with RAB7A. The effect of active RAB7A requires interactivity with TPCN2, as it was not observed in the presence of a mutant TPCN2 channel displaying normal ion conductance but defective in RAB7A interactivity.<sup>22</sup> In addition, a pharmacological RAB inhibitor<sup>58</sup> abolished the effects of iron overload on cell death in TPCN2-

expressing cells. Thus, and similar to the reported regulation of calcium conductance,<sup>22</sup> RAB7A activity also seems to modulate TPCN2-mediated events related to iron.

Interestingly, even though the increase in iron-mediated cell death in TPCN1-expressing cells was not potentiated in the presence of active RAB7A, coexpression of a dominant-negative RAB7A mutant defective in GTP binding did abolish iron-mediated cytotoxicity in both TPCN1- and TPCN2-expressing cells. This may be due to both TPCN channels requiring some basal RAB7A activity for proper functioning. In agreement with this, iron-induced cell death was not reverted with the dominant-negative RAB7A mutant in cells expressing the TPCN2 mutant defective in RAB7A binding. However, it remains possible that at least some beneficial effects of altering RAB7A activity are not related to directly modulating TPCN activity, but rather to additional effects on endolysosomal trafficking, positioning, acidity, autophagy or lysosome reformation, respectively.<sup>23,24,71-75</sup> In summary, our study provides evidence that NAADP-sensitive ion channels, and RAB7A activity modulate the iron storage capacity of endolysosomal organelles. The NAADP-mediated regulation of iron handling seems to involve both TPCN isoforms, highlighting the importance of those channels for proper intracellular iron homeostasis, and suggesting that NAADP antagonists and RAB7A inhibition may provide novel therapeutic approaches toward restoring cellular function in a variety of diseases associated with increased iron load.

## Materials and methods

### Reagents

Reagents included ammonium iron(III) citrate (Sigma Aldrich, F5879), ferric chloride (Sigma Aldrich, 44939), 2,2-bipyridyl (Sigma Aldrich, 366-18-7), 4,4-bipyridyl (Sigma Aldrich, 533-26-4), hydrogen peroxide (Sigma Aldrich, H10009), CID1067700 (Sigma Aldrich, 1067700), dynasore hydrate (Sigma Aldrich, D7693), bafilomycin A<sub>1</sub> (Sigma Aldrich, B1793), nigericin (Sigma Aldrich, N7143), iron dextran (Sigma Aldrich, D8517), BAPTA-AM (Invitrogen, B6769), acridine orange (Calbiochem, 113000), and torin 1 (Tocris Bioscience, 4247). Trans-Ned-19 and a cell-permeant version of NAADP (NAADP-AM) were synthesized as previously described.<sup>28,76</sup>

### DNA constructs and site-directed mutagenesis

Human TPCN1-mRFP, TPCN1<sup>L273P</sup>-mRFP, TPCN2-mRFP and TPCN2<sup>L265P</sup>-mRFP have been previously described.<sup>53,54,59</sup> Triply mutated TPCN2-mRFP (Q33A,V34A,P36A), shown to abolish binding of TPCN2 to RAB7A,<sup>22</sup> was generated by site-directed mutagenesis (QuikChange, Stratagene), and identity of the construct verified by DNA sequencing of the entire coding region. Cytosolic ro-GFP was a generous gift from S. Remington (University of Oregon, Eugene, USA), and MCOLN1 a generous gift from R. Puertollano (NIH, Bethesda, USA). Human GFP-RAB7A, GFP-RAB7A<sup>Q67L</sup> and GFP-RAB7A<sup>T22N</sup> have been previously described,<sup>59</sup> and were generous gifts from Dr. S. Ponnambalam (University of Leeds, Leeds, UK). HTT<sup>Q74</sup>-HA was a generous gift from Dr. D. Rubinsztein (Cambridge University, UK), LAMP1-GFP was a generous gift from Dr. E. DellAngelica (UCLA, USA), GFP-LC3B has been previously described,<sup>59</sup> the td-tag-LC3B construct was a generous gift from Dr. T. Johansen (University of Tromsø, Norway) and has been previously described,<sup>41</sup> shRNA plasmids coexpressing GFP to allow for easy identification of knockdown cells have been previously described,<sup>53,56</sup> and LAMP1-RFP was from Addgene (Addgene, 1817; deposited by Walter Mothes laboratory).

### Cell culture and transfections

HEK293T, HeLa, rat dopaminergic neuroendocrine PC12, and human primary dermal fibroblasts were cultured as previously described.<sup>59,77,78</sup> Human dopaminergic SH-SY5Y cells were cultured in DMEM/F-12 GLUTAMAX supplement (Gibco, 31331) containing 10% fetal bovine serum (Gibco, 10270), 2 mM glutamine, 100 U/ml penicillin and 100  $\mu$ l/ml streptomycin (Gibco, 15140) on collagen-coated plasticware. For collagen-coating, rat tail collagen type I (BD Biosciences, 354236; Lot. 2229980; 3.8 mg/ml solution) was added to 100-mm dishes (140  $\mu$ l) or to 35-mm wells (24  $\mu$ l), respectively, and evenly spread using a plastic spreader. Collagen was allowed to dry at room temperature for 30 minutes, followed by extensive rinsing with sterile H<sub>2</sub>O and medium before seeding cells, and cells were subcultured at a 1:3 ratio.

In all cases, cells at 70 to 80% confluency were transfected with Lipofectamine 2000 (Invitrogen, 12566014) according to the manufacturer's specifications for 4 h, followed by addition of fresh medium. Single transfections were performed using 3.5  $\mu$ g of

plasmid of interest and 10  $\mu$ l of Lipofectamine 2000. For double-transfections, 2.5  $\mu$ g of each plasmid were employed. Transfected cells were replated the next day at a 1:3 ratio onto poly-L-lysine-coated coverslips (Sigma Aldrich, P2636) in 6-well plates, followed by incubation with distinct compounds as indicated before analysis. To assure that the detected iron was intracellular and not accessible to an extracellular iron chelator, FAC-treated cultures were washed twice with phosphate-buffered saline (PBS; Gibco, 10010023) in the presence of deferoxamine (1 mM; Sigma Aldrich, D9533).<sup>79</sup>

### Cell extracts and western blotting

Cells were rinsed once in ice-cold PBS (Gibco, 10010023) and resuspended in 1 ml of lysis buffer (1% SDS [Sigma Aldrich, L4390] in PBS containing 1 mM PMSF, 1 mM Na<sub>3</sub>VO<sub>4</sub> and 5 mM NaF) per 100-mm dish, or 160  $\mu$ l of lysis buffer per well of a 6-well plate. Extracts were boiled for 5 min, sonicated and centrifuged at 10,000 g for 10 min at 4°C. Protein concentrations of supernatant fractions were estimated using the BCA assay (Thermo Fisher Scientific/Pierce Protein Biology, 23227). Samples (30  $\mu$ g) were resolved by SDS-PAGE, transferred onto polyvinylidene difluoride membranes (Amersham Hybond/GE Healthcare Life Sciences, 10600021), and probed with primary antibodies overnight at 4°C. Primary antibodies included mouse monoclonal anti-LAMP2 (8H4B4, 1:2000; Santa Cruz Biotechnology, 18822), mouse monoclonal anti-LAMP1 (H4A3 1:2000; Santa Cruz Biotechnology, 20011), mouse monoclonal anti-TUBA/ $\alpha$  tubulin (clone DM1A, 1:10,000; Sigma Aldrich, T6199), rabbit polyclonal anti-GFP (1:2000; Abcam, ab6556), rabbit polyclonal anti-LC3B (1:500; Cell Signaling Technologies, 2775), mouse monoclonal anti-SQSTM1 (1:500; BD Transduction Laboratories, 610833) and rabbit polyclonal anti-RFP (1:1000; Abcam, ab62341). Membranes were washed and incubated with secondary antibodies (anti-rabbit HRP-conjugated antibody (1:2000; Dako Cytomation, P0448) or anti-mouse HRP-conjugated antibody (1:2000; Dako Cytomation, P0447)) for 90 min at room temperature, followed by detection using ECL reagents (Roche Diagnostic GmbH; 120150200001). A series of timed exposures were undertaken to ensure that densitometric analyses were performed at exposures within the linear range, and films were scanned and densitometric analysis performed using QuantityOne (Bio-Rad).

### Determination of oxidative stress

Cellular oxidative stress levels were determined using the OxyBlot Protein Oxidation Detection Kit (Millipore EMD, S7150) essentially according to manufacturer's instructions. Briefly, 20  $\mu$ g of protein in lysis buffer (1% SDS in PBS containing 1 mM PMSF, 1 mM Na<sub>3</sub>VO<sub>4</sub>, 5 mM NaF, 2%  $\beta$ -mercaptoethanol) was incubated with 2,4-dinitrophenylhydrazine (DNPH) (included in the Detection Kit) for 15 min at room temperature. Samples were then neutralized before resolving them on a 10% SDS-PAGE gel, and transferred to nitrocellulose. Membranes were blocked in 5% milk, incubated with a rabbit anti-2,4-dinitrophenylhydrazine antibody (included in the Detection Kit) overnight at 4°C, followed by incubation with HRP-conjugated secondary antibodies

for 1 h. Immunocomplexes were visualized by chemiluminescence using the ECL method.

For determination of oxidation status in live cells, cells were transfected with ro-GFP<sup>38</sup> and treated with FAC as indicated. After 48 h, cells were washed twice with Hanks balanced salt solution (10 mM HEPES pH 7.4, 140 mM NaCl, 5 mM KCl, 1.3 mM MgCl<sub>2</sub>, 2 mM CaCl<sub>2</sub>, 1 g/l D-glucose), and imaged on a Leica TCS-SP5 confocal microscope (Leica Microsystems, Mannheim, Germany) using a 63X 1.4 NA oil UV objective (HCX PLAPO CS). Dual-excitation ratiometric imaging was performed at 400 and 480 nm, with emission wavelength at 535 nm, using Leica Applied Systems (LAS AF6000) image acquisition software. Fluorescence images were background-corrected by manual selection of background regions, and approximately 30 cells were measured for each condition. Images were taken at 1-min intervals, and where indicated, cells were perfused with buffer solution containing 1 mM H<sub>2</sub>O<sub>2</sub> or 1 mM DTT (ThermoFisher Scientific, R0861), respectively.

### Endolysosomal iron staining

Endolysosomal iron was stained using a modified sulphide-silver method using the FD RapidTimmStain Kit (FD Neurotechnologies, PK701) as previously described.<sup>11,57</sup> Briefly, cells grown on coverslips were either left untreated, or treated with 50  $\mu$ M FAC, 50  $\mu$ M FeCl<sub>2</sub> or 50  $\mu$ M Fe<sup>3+</sup>-dextran for 48 h. Under the latter conditions, endocytosed iron is expected to be localized exclusively to endolysosomes, and iron staining is typically observed in the vicinity of the nucleus. Cells were then washed in phosphate buffer and fixed with 2% glutaraldehyde in 0.1 M Na-cacodylate buffer (Sigma Aldrich, 70114) containing 0.1 M sucrose (pH 7.2) for 2 h at room temperature. Fixed cells were rinsed in warm distilled water, and sulphidated with sulphide solution for 10 min, followed by 3 incubations in 0.1 M phosphate buffer for 5 min each. The development was performed using FD RapidTimmStain Kit components for 20 min at 30°C in the dark, and the reaction stopped by transferring coverslips to warm distilled water. Cells were protected from light, and rinsed in distilled water 3 times for 5 min each. Coverslips were then dehydrated in graduated ethanol solutions (50%, 75%, absolute ethanol) and mounted using Canada Balsam (Sigma Aldrich, C1795). Phase contrast images were acquired using an Olympus IX81 microscope (Olympus Corporation, Tokyo, Japan) using a 100x objective, and iron-positive structures quantified using NIH ImageJ software.

### Iron dequenching imaging and quantification

Iron dequenching assays were performed essentially as described.<sup>11</sup> Briefly, cells were incubated in Hanks balanced salt solution (10 mM HEPES, 140 mM NaCl, 5 mM KCl, 1.3 mM MgCl<sub>2</sub>, 2 mM CaCl<sub>2</sub>, 1 g/l D-glucose, pH 7.4) and incubated with 20  $\mu$ M of the diacetate of Phen Green SK (Invitrogen, P14312), an iron-sensitive fluorescent indicator, for 20 min at 37°C. Phen Green SK fluorescence after loading is dependent on the intracellular concentrations of both the indicator itself and of chelatable iron which quenches the indicator's fluorescence. Therefore, after recording baseline fluorescence for 5 to 10 min, a nonfluorescent membrane-permeable iron chelator (2,2'-bipyridyl; 5 mM) was

added in excess to remove the iron from the Phen Green SK indicator, which leads to an increase in fluorescence. An analog of 2,2'-bipyridyl (4,4'-bipyridyl; 5 mM) without iron chelating capacity was used as negative control.

Fluorescence measurements were performed on an Olympus IX81 microscope using a 40x air objective. Green fluorescence of the Phen Green SK compound was excited at 488 nm, and emission collected through a 505 nm long-pass filter. Quantitative fluorescence measurements were performed by minimizing acquisition time to once per min so as to minimize photobleaching of the dye. For each experiment, an average of 30 to 40 cells were analyzed, with single cell fluorescence determined from confined regions of interest. Because many variables including dye loading can contribute to the variation of basal fluorescence of Phen Green SK, the normalized change of fluorescence (peak  $\Delta F/F_0$ ) was used as readout to estimate the change in cytosolic iron levels.<sup>11</sup>

### Acridine orange staining

Cells were cultured on polylysine-coated 35-mm glass-bottom dishes (IBIDI Biosciences, 81156), and either left untreated or treated with 50  $\mu$ M FAC or 50  $\mu$ M FeCl<sub>2</sub> for 48 h, or with 400 nM BAF (2h) or 25  $\mu$ M nigericin (5 min) as indicated. Cells were loaded with 5  $\mu$ g/ml acridine orange (AO) in complete medium for 15 min at 37°C, and images acquired on a Leica TCS-SP5 confocal microscope using a 63X 1.4 NA oil UV objective (HCX PLAPO CS) and single excitation (488 nm Argon Laser line and 655 to 721 nm and 508 to 548 nm emission band passes, respectively), and images quantified using NIH ImageJ software.

### Immunocytochemistry, quantitative image analysis and determination of apoptosis

For immunocytochemistry, transfected cells were replated at a 1:3 ratio onto coverslips and processed at the indicated times after transfection essentially as described.<sup>59,78</sup> Primary antibodies included a mouse monoclonal anti-LAMP2 antibody (1:50; Santa Cruz Biotechnology, 18822), a mouse monoclonal anti-LAMP1 antibody (1:100; Santa Cruz Biotechnology, 20011), a mouse monoclonal anti-EEA1 antibody (1:100; BD Transduction Laboratories, 610457), a mouse monoclonal anti-TSG101 antibody (1:100; Abcam, ab30871), a mouse monoclonal anti-Flag antibody (1:500; Sigma Aldrich, F1804), and a rabbit polyclonal anti-HA antibody (1:100; Sigma Aldrich, H6908). Secondary antibodies included goat anti-rabbit or goat anti-mouse Alexa Fluor 488-conjugates or Alexa Fluor 555-conjugates (1:1000; Invitrogen, A11034, A21428, A11001, A21422). Cells were mounted using ProLong Gold AntiFade mounting medium (Invitrogen, P36930), and images acquired on a Leica TCS-SP5 confocal microscope using a 63X 1.4 NA oil UV objective (HCX PLAPO CS). Images were collected using single excitation for each wavelength separately (488 nm Argon Laser line and a 500 to 545 nm emission band pass; HeNe Laser line and a 556 to 673 nm emission band pass; 405 nm UV diode and a 422 to 466 nm emission band pass (12.5% intensity)). 10 to 15 image sections of selected areas were acquired with a step size of 0.3  $\mu$ m, and z-stack images analyzed and processed using

Leica Applied Systems (LAS AF6000) image acquisition software. The same laser intensity was used for image acquisition of individual experiments.

For live cell fluorescence microscopy, transfected cells were reseeded onto 35-mm glass-bottom dishes the following day and imaged on a Leica TCS-SP5 confocal microscope using a 63X 1.4 NA oil UV objective (HCX PLAPO CS) as described above.

Autophagic activity was evaluated as previously described<sup>59,77</sup> by quantifying the average number of GFP-LC3B puncta per cell, or in the case of td-tag-LC3B experiments, the average number of both yellow and red structures per cell. Quantifications were performed from images acquired on a Leica TCS-SP5 confocal microscope using a 63X 1.4NA oil UV objective as described above. To determine the number and size of intracellular structures per cell, cells were circled, and a modified NIH ImageJ macro (GFP-LC3 macro) was employed as previously described.<sup>59</sup> For each condition per experiment, maximal intensity projections of an average of 20 independent cells were analyzed.

For detection of apoptosis, fixed cells were mounted using mounting medium containing DAPI (Vector Laboratories, H1200) and visualized on a Zeiss microscope (Zeiss International, Göttingen, Germany) using a 100x oil-immersion objective. For each experiment, 100 cells from random fields were quantified, and condensed or fragmented nuclei scored as apoptotic cells.

### Human tissue samples, cell extracts and atomic absorption spectroscopy

Freshly frozen brain samples from deceased human subjects were collected at autopsy following informed consent from the next of kin under a protocol approved by the local ethics committee. Metal analysis using atomic absorption spectroscopy was performed essentially as described.<sup>80</sup> Frozen substantia nigra samples (0.07 g) from 5 healthy controls and 5 age-matched Lewy body disease patients were homogenized in 500  $\mu$ l chilled lysis buffer containing pure HNO<sub>3</sub> at 65°C for 2 h. Samples were diluted 1:10 in double-distilled water and assayed on an atomic absorption spectrometer (AAFlame, AA800, S/N8566, Perkin Elmer, Norwalk, USA). The remainder of the sample was centrifuged at 3,500 g for 30 min at 4°C, and the supernatant fraction analyzed for total protein concentration using a Bradford assay (Thermo Scientific, 23227). Total iron content of each sample was measured in triplicate, and the concentrations determined from the standard curve were normalized to protein concentration or wet tissue weight. FAC-treated cells were pelleted, pellets resuspended in lysis buffer containing pure HNO<sub>3</sub> at 65°C for 2 h, and processed as described above.

### Statistical analysis

Data are represented as mean  $\pm$  s.e.m. Statistical comparisons were made using analysis of variance (ANOVA), and post-hoc Bonferroni analysis. A *P* value < 0.05 was considered statistically significant.

### Abbreviations

AO	acridine orange
BAF	bafilomycin A <sub>1</sub>
DAPI	4,6-diamidino-2-phenylindol dihydrochloride
DNA	deoxyribose nucleic acid
FAC	ferric ammonium citrate
GFP	green fluorescent protein
LAMP	lysosomal-associated membrane protein
MAP1LC3B/LC3B	microtubule-associated protein 1 light chain 3B
MCOLN/TRPML	mucolipin
NAADP	nicotinic adenine dinucleotide phosphate
RFP	red fluorescent protein
ro-GFP	reduction-oxidation-sensitive GFP
SDS	sodium dodecyl sulfate
SQSTM1/p62	sequestosome 1
TPCN	2-pore channel
TUBA	$\alpha$ tubulin

### Disclosure of potential conflicts of interest

No potential conflicts of interest were disclosed.

### Acknowledgments

The authors are grateful to Drs. D. Rubinsztein (University of Cambridge, UK), E. DellAngelica (UCLA, USA), S. Remington (University of Oregon, USA) and R. Puertollano (NIH, Bethesda, USA) for providing critical reagents. We thank L. Montosa for technical support with microscopy.

### Funding

This work was supported by funding from FEDER, The Spanish Ministry of Economy and Competitiveness (MINECO; SAF2014-58653-R), the Foundation BBVA and the Michael J. Fox Foundation. B.F. was supported by CEI Biotic Granada (CAEP2-13) and by a Juan de la Cierva Fellowship (JCI-2010-07703).

### References

- Ward RJ, Zucca FA, Duyn JH, Crichton RR, Zecca L. The role of iron in brain ageing and neurodegenerative disorders. *Lancet Neurol* 2014; 13:1045-60; PMID:25231526; [http://dx.doi.org/10.1016/S1474-4422\(14\)70117-6](http://dx.doi.org/10.1016/S1474-4422(14)70117-6)
- Dusek P, Jankovic J, Le W. Iron dysregulation in movement disorders. *Neurobiol Dis* 2012; 46:1-18; PMID:22266337; <http://dx.doi.org/10.1016/j.nbd.2011.12.054>
- Hentze MW, Muckenthaler MU, Galy B, Camaschella C. Two to tango: regulation of Mammalian iron metabolism. *Cell* 2010; 142:24-38; PMID:20603012; <http://dx.doi.org/10.1016/j.cell.2010.06.028>
- Blaby-Haas CE, Merchant SS. Lysosome-related organelles as mediators of metal homeostasis. *J Biol Chem* 2014; 289:28129-36; PMID:25160625; <http://dx.doi.org/10.1074/jbc.R114.592618>
- Nixon RA, Yang DS, Lee JH. Neurodegenerative lysosomal disorders: a continuum from development to late age. *Autophagy* 2008; 4:590-9; PMID:18497567; <http://dx.doi.org/10.4161/auto.6259>
- Grimm C, Hassan S, Wahl-Schott C, Biel M. Role of TRPML and two-pore channels in endolysosomal cation homeostasis. *J Pharmacol Exp Ther* 2012; 342:236-44; PMID:22518024; <http://dx.doi.org/10.1124/jpet.112.192880>
- Patel S. Function and dysfunction of two-pore channels. *Sci Signal* 2015; in the press; PMID:AMBIGUOUS

- [8] Puertollano R, Kiselyov K. TRPMLs: in sickness and in health. *Am J Physiol Renal Physiol* 2009; 296:F1245-54; PMID:19158345; <http://dx.doi.org/10.1152/ajprenal.90522.2008>
- [9] Cang C, Zhou Y, Navarro B, Seo YJ, Aranda K, Shi L, Battaglia-Hsu S, Nissim I, Clapham DE, Ren D. mTOR regulates lysosomal ATP-sensitive two-pore Na<sup>+</sup> channels to adapt to metabolic state. *Cell* 2013; 152:778-90; PMID:23394946; <http://dx.doi.org/10.1016/j.cell.2013.01.023>
- [10] Wang X, Zhang X, Dong XP, Samie M, Li X, Cheng X, Goschka A, Shen D, Zhou Y, Harlow J, et al. TPC proteins are phosphoinositide-activated sodium-selective ion channels in endosomes and lysosomes. *Cell* 2012; 151:372-83; PMID:23063126; <http://dx.doi.org/10.1016/j.cell.2012.08.036>
- [11] Dong XP, Cheng X, Mills E, Delling M, Wang F, Kurz T, Xu H. The type IV mucopolipidosis-associated protein TRPML1 is an endolysosomal iron release channel. *Nature* 2008; 455:992-6; PMID:18794901; <http://dx.doi.org/10.1038/nature07311>
- [12] Eichelsdoerfer JL, Evans JA, Slangenaupt SA, Cuajungco MP. Zinc dys-homeostasis is linked with the loss of mucopolipidosis IV-associated TRPML1 ion channel. *J Biol Chem* 2010; 285:34304-8; PMID:20864526; <http://dx.doi.org/10.1074/jbc.C110.165480>
- [13] Kiselyov K, Colletti GA, Terwilliger A, Ketchum K, Lyons CW, Quinn J, Muallem S. TRPML: transporters of metals in lysosomes essential for cell survival? *Cell Calcium* 2011; 50:288-94; PMID:21621258; <http://dx.doi.org/10.1016/j.ceca.2011.04.009>
- [14] Ruas M, Davis LC, Chen CC, Morgan AJ, Chuang KT, Walseth TF, Grimm C, Garnham C, Powell T, Platt N, et al. Expression of Ca<sup>2+</sup>-permeable two-pore channels rescues NAADP signalling in TPC-deficient cells. *EMBO J* 2015; 34:1743-58; pii: e201490009; PMID:25872774
- [15] Pitt SJ, Lam AK, Rietdorf K, Galione A, Sitsapesan R. Reconstituted human TPC1 is a proton-permeable ion channel and is activated by NAADP or Ca<sup>2+</sup>. *Sci Signal* 2014; 7(326):ra46; PMID:24847115; <http://dx.doi.org/10.1126/scisignal.2004854>
- [16] Calcraft PJ, Ruas M, Pan Z, Cheng X, Arredouani A, Hao X, Tang J, Rietdorf K, Teboul L, Chuang KT, et al. NAADP mobilizes calcium from acidic organelles through two-pore channels. *Nature* 2009; 459:596-600; PMID:19387438; <http://dx.doi.org/10.1038/nature08030>
- [17] Zong X, Schieder M, Cuny H, Fenske S, Gruner C, Rötzer K, Griesbeck O, Harz H, Biel M, Wahl-Schott C. The two-pore channel TPC2 mediates NAADP-dependent Ca<sup>2+</sup>-release from lysosomal stores. *Pflugers Arch* 2009; 458:891-9; PMID:19557428; <http://dx.doi.org/10.1007/s00424-009-0690-y>
- [18] Walseth TF, Lin-Moshier Y, Jain P, Ruas M, Parrington J, Galione A, Marchant JS, Slama JT. Photoaffinity labeling of high affinity nicotinic acid adenine dinucleotide phosphate (NAADP)-binding proteins in sea urchin egg. *J Biol Chem* 2012; 287:2308-15; PMID:22117077; <http://dx.doi.org/10.1074/jbc.M111.306563>
- [19] Lin-Moshier Y, Walseth TF, Churamani D, Davidson SM, Slama JT, Hooper R, Brailoiu E, Patel S, Marchant JS. Photoaffinity labeling of nicotinic acid adenine dinucleotide phosphate (NAADP) targets in mammalian cells. *J Biol Chem* 2012; 287:2296-307; PMID:22117075; <http://dx.doi.org/10.1074/jbc.M111.305813>
- [20] Guse AH. Linking NAADP to ion channel activity: a unifying hypothesis. *Sci Signal* 2012; 5:pe18; PMID:22534131; <http://dx.doi.org/10.1126/scisignal.2002890>
- [21] Jha A, Ahuja M, Patel S, Brailoiu E, Muallem S. Convergent regulation of the lysosomal two-pore channel-2 by Mg<sup>2+</sup>, NAADP, PI(3,5)P, and multiple protein kinases. *EMBO J* 2014; 33:501-11; PMID:24502975; <http://dx.doi.org/10.1002/embj.201387035>
- [22] Lin-Moshier Y, Keebler MV, Hooper R, Boulware MJ, Liu X, Churamani D, Aboud ME, Walseth TF, Brailoiu E, Patel S, et al. The Two-pore channel (TPC) interactome unmasks isoform-specific roles for TPCs in endolysosomal morphology and cell pigmentation. *Proc Natl Acad Sci U S A* 2014; 111:13087-92; PMID:25157141; <http://dx.doi.org/10.1073/pnas.1407004111>
- [23] Vitelli R, Santillo M, Lattero D, Chiariello M, Bifulco M, Bruni CB, Bucci C. Role of the small GTPase Rab7 in the late endocytic pathway. *J Biol Chem* 1997; 272:4391-7; PMID:9020161; <http://dx.doi.org/10.1074/jbc.272.7.4391>
- [24] Bucci C, Thomsen P, Nicoziani P, McCarthy J, van Deurs B. Rab7: a key to lysosome biogenesis. *Mol Biol Cell* 2000; 11:467-80; PMID:10679007; <http://dx.doi.org/10.1091/mbc.11.2.467>
- [25] Hyttinen JM, Niittykoski M, Salminen A, Kaarniranta K. Maturation of autophagosomes and endosomes: a key role for Rab7. *Biochim Biophys Acta* 2013; 1833:503-10; PMID:23220125; <http://dx.doi.org/10.1016/j.bbamcr.2012.11.018>
- [26] Ruas M, Rietdorf K, Arredouani A, Davis LC, Lloyd-Evans E, Koegel H, Funnell TM, Morgan AJ, Ward JA, Watanabe K, et al. Purified TPC isoforms form NAADP receptors with distinct roles for Ca(2+) signaling and endolysosomal trafficking. *Curr Biol* 2010; 20:703-9; PMID:20346675; <http://dx.doi.org/10.1016/j.cub.2010.02.049>
- [27] Marchant JS, Patel S. Two-pore channels at the intersection of endolysosomal membrane traffic. *Biochem Soc Trans* 2015; 43:434-41; PMID:26009187; <http://dx.doi.org/10.1042/BST20140303>
- [28] Naylor E, Arredouani A, Vasudevan SR, Lewis AM, Parkesh R, Mizote A, Rosen D, Thomas JM, Izumi M, Ganesan A, et al. Identification of a chemical probe for NAADP by virtual screening. *Nat Chem Biol* 2009; 5:220-6; PMID:19234453; <http://dx.doi.org/10.1038/nchembio.150>
- [29] Ayton S, Lei P. Nigral iron elevation is an invariable feature of Parkinson's disease and is a sufficient cause of neurodegeneration. *Biomed Res Int* 2014; 2014:581256; PMID:24527451; <http://dx.doi.org/10.1155/2014/581256>
- [30] Sofic E, Paulus W, Jellinger K, Riederer P, Youdim MB. Selective increase of iron in substantia nigra zona compacta of parkinsonian brains. *J Neurochem* 1991; 56:978-82; PMID:1704426; <http://dx.doi.org/10.1111/j.1471-4159.1991.tb02017.x>
- [31] Funke C, Schneider SA, Berg D, Kell DB. Genetics and iron in the systems biology of Parkinson's disease and some related disorders. *Neurochem Int* 2013; 62:637-52; PMID:23220386; <http://dx.doi.org/10.1016/j.neuint.2012.11.015>
- [32] Lane DJ, Merlot AM, Huang ML, Bae DH, Jansson PJ, Sahni S, Kalinowski DS, Richardson DR. Cellular iron uptake, trafficking and metabolism: Key molecules and mechanisms and their roles in disease. *Biochim Biophys Acta* 2015; 1853:1130-44; PMID:25661197; <http://dx.doi.org/10.1016/j.bbamcr.2015.01.021>
- [33] Rouault TA. Iron metabolism in the CNS: implications for neurodegenerative diseases. *Nat Rev Neurosci* 2013; 14:551-64; PMID:23820773; <http://dx.doi.org/10.1038/nrn3453>
- [34] Mills E, Dong XP, Wang F, Xu H. Mechanisms of brain iron transport: insight into neurodegeneration and CNS disorders. *Future Med Chem* 2010; 2:51-64; PMID:20161623; <http://dx.doi.org/10.4155/fmc.09.140>
- [35] Salvador GA, Oteiza PI. Iron overload triggers redox-sensitive signals in human IMR-32 neuroblastoma cells. *Neurotoxicology* 2011; 32:75-82; PMID:21130806; <http://dx.doi.org/10.1016/j.neuro.2010.11.006>
- [36] You LH, Li F, Wang L, Zhao SE, Wang SM, Zhang LL, Zhang LH, Duan XL, Yu P, Chang YZ. Brain iron accumulation exacerbates the pathogenesis of MPTP-induced Parkinson's disease. *Neuroscience* 2015; 284:234-46; PMID:25301748; <http://dx.doi.org/10.1016/j.neuroscience.2014.09.071>
- [37] Kirchhausen T, Macia E, Pelish HE. Use of dynasore, the small molecule inhibitor of dynamin, in the regulation of endocytosis. *Methods Enzymol* 2008; 438:77-93; PMID:18413242; [http://dx.doi.org/10.1016/S0076-6879\(07\)38006-3](http://dx.doi.org/10.1016/S0076-6879(07)38006-3)
- [38] Dooley CT, Dore TM, Hanson GT, Jackson WC, Remington SJ, Tsien RY. Imaging dynamic redox changes in mammalian cells with green fluorescent protein indicators. *J Biol Chem* 2004; 279:22284-93; PMID:14985369; <http://dx.doi.org/10.1074/jbc.M312847200>
- [39] Filomeni G, De Zio D, Ceconi F. Oxidative stress and autophagy: the clash between damage and metabolic needs. *Cell Death Differ* 2015; 22:377-88; PMID:25257172; <http://dx.doi.org/10.1038/cdd.2014.150>
- [40] Bjorkoy G, Lamark T, Pankiv S, Overvatn A, Brech A, Johansen T. Monitoring autophagic degradation of p62/SQSTM1. *Methods Enzymol* 2009; 452:181-97; PMID:19200883; [http://dx.doi.org/10.1016/S0076-6879\(08\)03612-4](http://dx.doi.org/10.1016/S0076-6879(08)03612-4)
- [41] Pankiv S, Clausen TH, Lamark T, Brech A, Bruun JA, Overvatn A, Bjorkoy G, Johansen T. p62/SQSTM1 binds directly to Atg8/LC3 to facilitate degradation of ubiquitinated protein aggregates by autophagy. *J Biol Chem* 2007; 282:24131-45; PMID:17580304; <http://dx.doi.org/10.1074/jbc.M702824200>

- [42] Thoreen CC, Kang SA, Chang JW, Liu Q, Zhang J, Gao Y, Reichling LJ, Sim T, Sabatini DM, Gray NS. An ATP-competitive mammalian target of rapamycin inhibitor reveals rapamycin-resistant functions of mTORC1. *J Biol Chem* 2009; 284:8023-8032; PMID:19150980; <http://dx.doi.org/10.1074/jbc.M900301200>
- [43] Lichtenberg M, Mansilla A, Zecchini VR, Fleming A, Rubinsztein DC. The Parkinson's disease protein LRRK2 impairs proteasome substrate clearance without affecting proteasome catalytic activity. *Cell Death Dis* 2011; 2:e196; PMID:21866175; <http://dx.doi.org/10.1038/cddis.2011.81>
- [44] Nixon RA. The role of autophagy in neurodegenerative disease. *Nat Med* 2013; 19:983-97; PMID:23921753; <http://dx.doi.org/10.1038/nm.3232>
- [45] Klionsky DJ. Neurodegeneration: good riddance to bad rubbish. *Nature* 2006; 441:819-20; PMID:16778876; <http://dx.doi.org/10.1038/441819a>
- [46] Shintani T, Klionsky DJ. Autophagy in health and disease: a double-edged sword. *Science* 2004; 306:990-5; PMID:15528435; <http://dx.doi.org/10.1126/science.1099993>
- [47] Butler D, Nixon RA, Bahr BA. Potential compensatory responses through autophagic/lysosomal pathways in neurodegenerative diseases. *Autophagy* 2006; 2:234-7; PMID:16874061; <http://dx.doi.org/10.4161/auto.2729>
- [48] Rubinsztein DC. The roles of intracellular protein-degradation pathways in neurodegeneration. *Nature* 2006; 443:780-6; PMID:17051204; <http://dx.doi.org/10.1038/nature05291>
- [49] Mizushima N, Levine B, Cuervo AM, Klionsky DJ. Autophagy fights disease through cellular self-digestion. *Nature* 2008; 451:1069-75; PMID:18305538; <http://dx.doi.org/10.1038/nature06639>
- [50] Falcón-Pérez JM, Nazarian R, Sabatti C, Dell'Angelica EC. Distribution and dynamics of Lamp1-containing endocytic organelles in fibroblasts deficient in BLOC-3. *J Cell Sci* 2005; 118:5243-55; PMID:Can't; <http://dx.doi.org/10.1242/jcs.02633>
- [51] Boya P, Kroemer G. Lysosomal membrane permeabilization in cell death. *Oncogene* 2008; 27:6434-51; PMID:18955971; <http://dx.doi.org/10.1038/ncr.2008.310>
- [52] Soyombo AA, Tjon-Kon-Sang S, Rbaibi Y, Bashllari E, Biscaglia J, Muallem S, Kiselyov K. TRP-ML1 regulates lysosomal pH and acidic lysosomal lipid hydrolytic activity. *J Biol Chem* 2006; 281:7294-301; PMID:16361256; <http://dx.doi.org/10.1074/jbc.M508211200>
- [53] Brailoiu E, Churamani D, Cai X, Schrlau MG, Brailoiu GC, Gao X, Hooper R, Boulware MJ, Dun NJ, Marchant JS, et al. Essential requirement for two-pore channel 1 in NAADP-mediated calcium signaling. *J Cell Biol* 2009; 186:201-9; PMID:19620632; <http://dx.doi.org/10.1083/jcb.200904073>
- [54] Brailoiu E, Rahman T, Churamani D, Prole DL, Brailoiu GC, Hooper R, Taylor CW, Patel S. An NAADP-gated two-pore channel targeted to the plasma membrane uncouples triggering from amplifying Ca<sup>2+</sup> signals. *J Biol Chem* 2010; 285:38511-6; PMID:20880839; <http://dx.doi.org/10.1074/jbc.M110.162073>
- [55] Yamaguchi S, Jha A, Li Q, Soyombo AA, Dickinson GD, Churamani D, Brailoiu E, Patel S, Muallem S. Transient receptor potential mucopolipin 1 (TRPML1) and two-pore channels are functionally independent organellar ion channels. *J Biol Chem* 2011; 286:22934-42; PMID:21540176; <http://dx.doi.org/10.1074/jbc.M110.210930>
- [56] Dionisio N, Albarrán L, López JJ, Berna-Erro A, Salido GM, Bobe R, Rosado JA. Acidic NAADP-releasable Ca(2+) compartments in the megakaryoblastic cell line MEG01. *Biochim Biophys Acta* 2011; 1813:1483-94; PMID:21601596; <http://dx.doi.org/10.1016/j.bbamcr.2011.05.005>
- [57] Zdolsek JM, Roberg K, Brunk UT. Visualization of iron in cultured macrophages: a cytochemical light and electron microscopy study using autometallography. *Free Radic Biol Med* 1993; 15:1-11; PMID:8359707; [http://dx.doi.org/10.1016/0891-5849\(93\)90120-J](http://dx.doi.org/10.1016/0891-5849(93)90120-J)
- [58] Agola JO, Hong L, Surviladze Z, Ursu O, Waller A, Strouse JJ, Simpson DS, Schroeder CE, Oprea TI, Golden JE, et al. A competitive nucleotide binding inhibitor: in vitro characterization of Rab7 GTPase inhibition. *ACS Chem Biol* 2012; 7:1095-108; PMID:22486388; <http://dx.doi.org/10.1021/cb3001099>
- [59] Gómez-Suaga P, Rivero-Ríos P, Fdez E, Blanca Ramírez M, Ferrer I, Aiastui A, López De Munain A, Hilfiker S. LRRK2 delays degradative receptor trafficking by impeding late endosomal budding through decreasing Rab7 activity. *Hum Mol Genet* 2014; 23:6779-96; PMID:Can't; <http://dx.doi.org/10.1093/hmg/ddu395>
- [60] Hockey LN, Kilpatrick BS, Eden ER, Lin-Moshier Y, Brailoiu GC, Brailoiu E, Futter CE, Schapira AH, Marchant JS, Patel S. Dysregulation of lysosomal morphology by pathogenic LRRK2 is corrected by TPC2 inhibition. *J Cell Sci* 2015; 128:232-8; PMID:25416817; <http://dx.doi.org/10.1242/jcs.164152>
- [61] Fares H, Greenwald I. Regulation of endocytosis by CUP-5, the *Caenorhabditis elegans* mucopolipin-1 homolog. *Nat Genet* 2001; 28:64-8; PMID:11326278
- [62] Myers BM, Prendergast FG, Holman R, Kuntz SM, LaRusso NF. Alterations in the structure, physicochemical properties, and pH of hepatocyte lysosomes in experimental iron overload. *J Clin Invest* 1991; 88:1207-15; PMID:1918375; <http://dx.doi.org/10.1172/JCI115423>
- [63] Berggren KL, Chen J, Fox J, Miller J, Dodds L, Dugas B, Vargas L, Lothian A, McAllum E, Volitakis I, et al. Neonatal iron supplementation potentiates oxidative stress, energetic dysfunction and neurodegeneration in the R6/2 mouse model of Huntington's disease. *Redox Biol* 2015; 4:363-74; PMID:25703232; <http://dx.doi.org/10.1016/j.redox.2015.02.002>
- [64] Chen J, Marks E, Lai B, Zhang Z, Duce JA, Lam LQ, Volitakis I, Bush AI, Hersch S, Fox JH. Iron accumulates in Huntington's disease neurons: protection by deferoxamine. *PLoS One* 2013; 8(10):e77023; PMID:24146952; <http://dx.doi.org/10.1371/journal.pone.0077023>
- [65] Asano T, Komatsu M, Yamaguchi-Iwai Y, Ishikawa F, Mizushima N, Iwai K. Distinct mechanisms of ferritin delivery to lysosomes in iron-depleted and iron-replete cells. *Mol Cell Biol* 2011; 31:2040-52; PMID:21444722; <http://dx.doi.org/10.1128/MCB.01437-10>
- [66] Dowdle WE, Nyfeler B, Nagel J, Elling RA, Liu S, Triantafellow E, Menon S, Wang Z, Honda A, Pardee G, et al. Selective VPS34 inhibitor blocks autophagy and uncovers a role for NCOA4 in ferritin degradation and iron homeostasis in vivo. *Nat Cell Biol* 2014; 16:1069-79; PMID:25327288; <http://dx.doi.org/10.1038/ncb3053>
- [67] Mancias JD, Wang X, Gygi SP, Harper JW, Kimmelman AC. Quantitative proteomics identifies NCOA4 as the cargo receptor mediating ferritinophagy. *Nature* 2014; 509:105-9; PMID:24695223; <http://dx.doi.org/10.1038/nature13148>
- [68] Shawki A, Knight PB, Maliken BD, Niespodzany EJ, Mackenzie B. H (+)-coupled divalent metal-ion transporter-1: functional properties, physiological roles and therapeutics. *Curr Top Membr* 2012; 70:169-214; PMID:23177986; <http://dx.doi.org/10.1016/B978-0-12-394316-3.00005-3>
- [69] Zhu MX, Ma J, Parrington J, Galione A, Evans AM. TPCs: endolysosomal channels for Ca<sup>2+</sup> mobilization from acidic organelles triggered by NAADP. *FEBS Lett* 2010; 584:1966-74; PMID:20159015; <http://dx.doi.org/10.1016/j.febslet.2010.02.028>
- [70] Chavrier P, Parton RG, Hauri HP, Simons K, Zerial M. Localization of low molecular weight GTP binding proteins to exocytic and endocytic compartments. *Cell* 1990; 62:317-29; PMID:2115402; [http://dx.doi.org/10.1016/0092-8674\(90\)90369-P](http://dx.doi.org/10.1016/0092-8674(90)90369-P)
- [71] Gutierrez MG, Munafó DB, Berón W, Colombo MI. Rab7 is required for the normal progression of the autophagic pathway in mammalian cells. *J Cell Sci* 2004; 117:2687-97; PMID:15138286; <http://dx.doi.org/10.1242/jcs.01114>
- [72] Jäger S, Bucci C, Tanida I, Ueno T, Kominami E, Saftig P, Eskelinen EL. Role for Rab7 in maturation of late autophagic vacuoles. *J Cell Sci* 2004; 117:4837-48; PMID:Can't; <http://dx.doi.org/10.1242/jcs.01370>
- [73] Hyttinen JM, Niittykoski M, Salminen A, Kaarniranta K. Maturation of autophagosomes and endosomes: a key role for Rab7. *Biochim Biophys Acta* 2013; 1833:503-10; PMID:23220125; <http://dx.doi.org/10.1016/j.bbamcr.2012.11.018>
- [74] Bento CF, Puri C, Moreau K, Rubinsztein DC. The role of membrane-trafficking small GTPases in the regulation of autophagy. *J Cell Sci* 2013; 126:1059-69; PMID:23620509; <http://dx.doi.org/10.1242/jcs.123075>
- [75] Yu L, McPhee CK, Zheng L, Mardones GA, Rong Y, Peng J, Mi N, Zhao Y, Liu Z, Wan F, et al. Termination of autophagy and reformation of lysosomes regulated by mTOR. *Nature* 2010; 465:942-6; PMID:20526321; <http://dx.doi.org/10.1038/nature09076>
- [76] Parkesh R, Lewis AM, Aley PK, Arredouani A, Rossi S, Tavares R, Vasudevan SR, Rosen D, Galione A, Dowden J, et al. Cell-permeant

- NAADP: a novel chemical tool enabling the study of Ca<sup>2+</sup> signalling in intact cells. *Cell Calcium* 2008; 43:531-8; PMID:17935780; <http://dx.doi.org/10.1016/j.ceca.2007.08.006>
- [77] Gómez-Suaga P, Luzón-Toro B, Churamani D, Zhang L, Bloor-Young D, Patel S, Woodman PG, Churchill GC, Hilfiker S. Leucine-rich repeat kinase 2 regulates autophagy through a calcium-dependent pathway involving NAADP. *Hum Mol Genet* 2012; 21:511-25; PMID:Can't; <http://dx.doi.org/10.1093/hmg/ddr481>
- [78] Fdez E, Martínez-Salvador M, Beard M, Woodman P, Hilfiker S. Transmembrane-domain determinants for SNARE-mediated membrane fusion. *J Cell Sci* 2010; 123:2473-80; PMID:20571052; <http://dx.doi.org/10.1242/jcs.061325>
- [79] Riemer J, Hoepken HH, Czerwinska H, Robinson SR, Dringen R. Colorimetric ferrozine-based assay for the quantitation of iron in cultured cells. *Anal Biochem* 2004; 331:370-5; PMID:15265744; <http://dx.doi.org/10.1016/j.ab.2004.03.049>
- [80] Lei P, Ayton S, Finkelstein DI, Spoerri L, Ciccosto GD, Wright DK, Wong BX, Adlard PA, Cherny RA, Lam LQ, et al. Tau deficiency induces parkinsonism with dementia by impairing APP-mediated iron export. *Nat Med* 2012; 18:291-5; PMID:22286308; <http://dx.doi.org/10.1038/nm.2613>